



HAL
open science

Night light polarization: modeling and observations of light pollution in the presence of aerosols and background skylight or airglow

Léo Bosse, Jean Lilensten, Nicolas Gillet, Colette Brogniez, Olivier Pujol, Sylvain Rochat, Alain Delboulbé, Stephane Curaba, Magnar G Johnsen

► To cite this version:

Léo Bosse, Jean Lilensten, Nicolas Gillet, Colette Brogniez, Olivier Pujol, et al.. Night light polarization: modeling and observations of light pollution in the presence of aerosols and background skylight or airglow. 2022. <hal-03550521>

HAL Id: hal-03550521

<https://hal.science/hal-03550521v1>

Preprint submitted on 1 Feb 2022

HAL is a multi-disciplinary open access archive for the deposit and dissemination of scientific research documents, whether they are published or not. The documents may come from teaching and research institutions in France or abroad, or from public or private research centers.

L'archive ouverte pluridisciplinaire HAL, est destinée au dépôt et à la diffusion de documents scientifiques de niveau recherche, publiés ou non, émanant des établissements d'enseignement et de recherche français ou étrangers, des laboratoires publics ou privés.



HAL Authorization

1 **Night light polarization: modeling and observations of light**
2 **pollution in the presence of aerosols and background skylight or**
3 **airglow**

4 **Léo Bosse¹, Jean Lilensten^{1,5}, Nicolas Gillet², Colette Brogniez³, Olivier Pujol³, Sylvain**
5 **Rochat¹, Alain Delboulbé¹, Stéphane Curaba¹, Magnar G. Johnsen⁴**

6 ¹Institut de Planétologie et d'Astrophysique de Grenoble (IPAG) CNRS – UGA, France

7 ²Univ. Grenoble Alpes, Univ. Savoie Mont Blanc, CNRS, IRD, UGE, ISTerre, 38000 Grenoble, France

8 ³Univ. Lille, CNRS, UMR 8518 – LOA – Laboratoire d'Optique Atmosphérique, F-59000 Lille, France

9 ⁴Tromsø Geophysical Observatory, UiT - the Arctic University of Norway, Tromsø, Norway

10 ⁵Honorary astronomer at Royal Observatory of Belgium, Brussels

11 **Key Points:**

- 12 • First polarized radiative transfer code for night light and atmospheric studies including
13 Lorenz-Mie and Rayleigh polarized scattering.
14 • Application to aerosols, light pollution and thermospheric nightglow studies.
15 • Validation through specific measurements at different wavelengths

Corresponding author: Léo Bosse, leo.bosse@univ-grenoble-alpes.fr

Abstract

Aurorae and nightglow are faint atmospheric emissions visible during night-time at several wavelengths. These emissions have been extensively studied but their polarization remains controversial. A great challenge is that light pollution from cities and scattering in the lower atmosphere interfere with polarization measurements. We introduce a new polarized radiative transfer model able to compute the polarization measured by a virtual instrument in a given nocturnal environment recreating real world conditions (atmospheric and aerosol profiles, light sources with complex geometries, terrain obstructions). The model, based on single scattering equations in the atmosphere, is tested on a few simple configurations to assess the effect of several key parameters in controlled environments. Our model constitutes a proof of concept for polarization measurements in nocturnal conditions, that calls for further investigations. In particular, we discuss how multiple-scattering (neglected in the present study) impacts our observations and their interpretation, and the future need for inter-calibrating the source and the polarimeter in order to optimally extract the information contained in this kind of measurements. The model outputs are compared to field measurements in five wavelengths. A convincing fit between the model predictions and observations is found in the three most constrained wavelengths despite the single scattering approximation. Several applications of our model are discussed that concern the polarization of aurorae, the impact of light pollution, or aerosols and air pollution measurements.

Plain Language Summary

The darkest night is not black. It is actually quite luminous: The upper atmosphere emits its own glow, called *nightglow*; there is also the light from the stars, that from artificial sources, and their possible reflections, on snow for example. All these lights are further scattered in the atmosphere by the air molecules and/or the aerosols (dust, ice crystals, droplets...). This scattering makes the light waves oscillate in a privileged direction: it becomes *polarized*. In this article, we use a dedicated instrument that we developed (a polarimeter), along with a numerical code called POMEROL that accounts for all the above sources. We show that polarization may be used for studying the nightglow, light pollution or aerosols, with several possible applications in ecology, atmospheric sciences and space weather.

1 Introduction

The main auroral emissions are due to the atomic oxygen and molecular ion nitrogen N_2^+ . The former produces the red (630 nm) and green (557.7 nm) light at the altitudes of about 220 and 110 km respectively. The latter emits in a large band amongst which the most prominent emissions are the blue (427.8 nm) and the purple (391.4 nm) radiation, around an altitude of 85 km. They mainly originate in the collisions between precipitated electrons and the ambient atmosphere (see for example Banks & Kockarts, 1973).

These emissions are pronounced at high latitudes, in the auroral ovals. At other latitudes, emissions of the upper atmosphere are called *nightglow* (Leinert et al., 1998). The literature is abundant and here we only refer to some recent works. They exist at all latitudes (Parihar et al., 2018). Their origin is due to chemical reactions (Plane et al., 2012) and collisions, either between neutral molecules or atoms, or between ambient ionospheric electrons and gases (Tashchilin & Leonovich, 2016). The drivers may be gravity waves (Vargas, 2019) or ionospheric currents (Dymond et al., 2019).

For the last decade, a serie of experiments have shown that the red emission, when measured from the ground, is polarized (Lilensten et al., 2016, and references herein). The direction of polarization for this red line was shown theoretically to be parallel to the magnetic field (Bommier et al., 2011). Correlations between variations in the magnetic field and in the angle of linear polarization (*AoLP*) had indeed been observed experimentally, but not systematically, with a first prototype of auroral polarimeter (Lilensten et al., 2008).

65 Recently, a new nightglow polarimeter has been developed in order to observe low radi-
66 ant flux emissions (i.e. not limited to bright aurorae). It also allows to target simultaneously
67 several atmospheric emissions (for a full description, see Bosse et al., 2020). Three findings
68 by Bosse et al. (2020) lead us to reconsider our first understanding of the upper atmosphere
69 polarization:

- 70 • All of the four auroral emission lines appear polarized when measured from the ground,
- 71 • Although in several circumstances this polarization appears to be linked to the local
72 magnetic activity and to the state of the ionosphere, it is far from being systematically
73 aligned on the apparent direction of the magnetic field, as foreseen theoretically,
- 74 • Light pollution from nearby cities significantly impacts, via scattering, the polarization
75 measurements.

76 These series of observations questioned the geophysical origin of the polarization: how much
77 is it affected by light pollution scattering in the lower atmosphere? Are auroral lights polarized
78 at the emission or during their propagation toward to the instrument? To answer these ques-
79 tions, it is necessary to develop a polarized radiative transfer code able to account for sources
80 potentially spread all over both the sky and the ground.

81 In this paper, we describe the first code developed to this purpose, called ‘POMEROL’
82 (standing for ‘POLarisation par Mie Et Rayleigh des Objets Lumineux’).. It takes into ac-
83 count the light emitted in the upper atmosphere, as well as all possible pollution sources on
84 the ground. We present some examples of applications, with comparisons to geophysical
85 data obtained in the French Alps. In this paper the code is restricted to a single scattering
86 approximation (SSA). The goal here is to prove the feasibility of night-time polarisation mea-
87 surements. Thus, the model is currently kept as simple as possible. We show that even in this
88 relatively simple configuration, it is possible to reproduce quite well the measurements and to
89 deduce physical parameters behind the polarization. However, we also discuss the limitations
90 of this first approach, and what improvements could be brought by considering a polarized
91 multiple scattering radiative scheme. In this first paper about night-time polarization, we think
92 it is useful to know what the single scattering approximation can give before diving into the
93 complexity of multiple scattering. We will see that the SSA can already catch the essence
94 of the physics at hand. Our study paves the way to future investigations of the night-light
95 polarization, and calls for evolution of the model, including in particular multiple scattering.

96 Such a code is not designed only to better understand the upper atmosphere. It could
97 also help to characterize aerosols in a passive experimental way in the absence of the moon
98 or the sun. It may also lead to more accurate monitoring of light pollution, which represents
99 a growing concern over the last decades. The area covered by light from human origin is
100 spreading, along with its impacts on life (Grubisic et al., 2018), energy consumption (Kyba
101 et al., 2017) or astronomy. Among the literature displaying a varied list of negative effects,
102 we can cite the insect population decline and the “Ecological Armageddon” (Grubisic et al.,
103 2018) or health issues (Garcia-Saenz et al., 2018; Zielinska-Dabkowska, 2018). Most of the
104 studies concentrates on the exposure rate and magnitude. However, we lack studies on light
105 pollution polarization (Horvath et al., 2009; Kyba et al., 2011). Yet it plays an important role
106 for vast groups of insects that use it to navigate.

107 Below, we briefly describe the instrument in Section 2. We then present the principles
108 of the radiative transfer model in Section 3.2 (the full details are given in Appendix A). Next
109 we provide in Section 4 a series of synthetic experiments in order to assess the influence of
110 the input parameters: effect of a localized source on the ground, of atmospheric properties
111 (ozone, aerosols) and of multiple scattering. In Section 5, we compare the measurements
112 from an experimental campaign at mid-latitude to the model outputs. Finally, we discuss our
113 findings in Section 6.

2 Description of the polarimeter

Here is a brief overview of the experimental set-up. The polarimeter used in this study has been fully described in Bosse et al. (2020). We therefore only recall here its basics.

The incoming light along the line of sight is filtered through a narrow optical filter (of 2 nm width for the red line and 10 nm width for all other lines). Behind it a polarizing lens rotates at 2 Hz. The light passing the lens then hits a photomultiplier and is converted into an electrical current with a 1 kHz sampling rate. Data are smoothed over a given time window during which the polarization is assumed constant (10 seconds for all data presented here). A lock-in analysis is performed in real time. This powerful method allows a fast and accurate computation of the polarization. However, when the degree of linear polarization (*DoLP*) becomes too small, typically below 0.5%, the *AoLP* can hardly be computed and becomes very noisy. Both the *DoLP* and *AoLP* have been calibrated, but not the radiant flux.

We note F_0 the incident radiant flux received at a given wavelength. The *DoLP* ranges between 0 and 1 (or, in the figures, 0 to 100%), and we define the *AoLP* with respect to the vertical (0° being upward, $\pm 90^\circ$ horizontal as it is π -periodic). φ_t is the angle of the polarizing filter with the vertical at time t . We suppose F_0 , *DoLP* and *AoLP* to not change during one rotation of the polarizing filter. From basic optics, the radiant flux passing through the polarizing filter can be decomposed in two parts: a polarized one that varies as $\cos^2(\varphi_t - AoLP)$, and an unpolarized part, assumed to be constant over one rotation. For an incident radiant flux F_0 , the polarized and unpolarized fluxes are

$$\begin{cases} F_0^{pola} = DoLP \times F_0 \\ F_0^{unpola} = (1 - DoLP) \times F_0 \end{cases} . \quad (1)$$

Following Malus Law, after the polarizing filter they become

$$\begin{cases} F_t^{pola} = F_0^{pola} \cos^2(\varphi_t - AoLP) \\ F_t^{unpola} = F_0^{unpola} / 2 \end{cases} . \quad (2)$$

The 1/2 factor on the unpolarized radiant flux comes from the averaging of Malus law on all *AoLP*. The radiant flux measured at time t can therefore be written as:

$$F_t = F_t^{pola} + F_t^{unpola} = F_0 \left(DoLP \times \cos^2(\varphi_t - AoLP) + \frac{1 - DoLP}{2} \right) . \quad (3)$$

Over one rotation of period T_r , this allows computing the Stokes parameters in spherical coordinates as:

$$\begin{cases} I = \frac{1}{T_r} \int_0^{T_r} F_t dt \\ Q = \frac{1}{T_r} \int_0^{T_r} F_t \cos 2\varphi_t dt \\ U = -\frac{1}{T_r} \int_0^{T_r} F_t \sin 2\varphi_t dt \end{cases} . \quad (4)$$

Note that we do not consider circularly polarized light, such that the last Stokes parameter $V = 0$. Injecting (3) in (4), one deduces the polarization parameters:

$$\begin{cases} F_0 = 2I \\ DoLP = \frac{2}{I} \sqrt{Q^2 + U^2} \\ AoLP = \frac{1}{2} \arctan \left(\frac{U}{Q} \right) \end{cases} \quad (5)$$

The data may be smoothed over time by averaging I , Q and U over the desired number of rotations and then calculating the corresponding polarization values.

148 **3 The radiative transfer model**

149 In order to interpret the data from the instrument described in Section 2, we need to
 150 solve the polarized radiative transfer equations. This is the goal of the POMEROL code. We
 151 describe its inputs in Section 3.1 while the polarized radiative transfer equations are summa-
 152 rized in Section 3.2 and fully described in Appendix A. For the purpose of the present study,
 153 our analysis is based on single scattering. The limits of this approximation are discussed later
 154 on in Section 4.4. We aim at modeling the polarization observations under different configu-
 155 rations. We thus consider potentially several sources of light: direct light (from the nightglow,
 156 or the star-light), single scattered light (e.g. from cities, or auroral lights at high latitude).

157 **3.1 Inputs of the model**

158 **3.1.1 Instrument related entries**

159 The experimental characteristics are the first inputs, in particular the surface $\Sigma = 20 \text{ cm}^2$
 160 of the detector and its half aperture angle $\varepsilon = 1^\circ$, as well as its geographical position (latitude,
 161 longitude and altitude) and its pointing direction. This latter is defined by the elevation e
 162 (angle between the horizontal and the line of sight) and the azimuth a , reckoned with respect
 163 to the North, positive Eastward, i.e. clockwise rotation. One can specify discrete azimuths and
 164 elevations, or span over an *almucantar* (i.e. a full rotations in azimuth at a constant elevation)
 165 automatically.

166 **3.1.2 Cities and pollution map**

167 The model also takes as input a light pollution map. These are ground images of Earth
 168 at night produced by the NOAA Earth Observations Group, using satellite data from the Vis-
 169 ible Infrared Imaging Radiometer Suite Day/Night Band. These images sum the emissions
 170 for wavelengths from 500 to 900 nm (Mills et al., 2013; Miller et al., 2013). The maps are
 171 processed by their authors to remove ephemeral light and are averaged over one year. They
 172 are provided by their authors in two modes, with the minimum emission set to zero or not. At
 173 high latitudes, auroral light are not always removed with other ephemeral lights, thus emission
 174 maps are overestimated. To better suppress the auroral contribution to the ground emission
 175 map, we use the second mode. At mid-latitude, the difference is minimal and we use the same
 176 mode for consistency. We use the most recent release from 2016. The ground emission are in
 177 units of $\text{nW/m}^2/\text{sr}$.

178 The map is centered on the instrument in polar coordinates (see Figure 8). The max-
 179 imum range from the instrument (typically up to 200 km) and the number of bins (the best
 180 resolution being that of the map, namely 46 m) are adjustable parameters. To reduce artifacts
 181 due to digitization, the size of the bins increases with the square root of the distance to the
 182 instrument.

183 We can also consider instead synthetic emission maps. For example, these may consist
 184 of a point source of given radiance at a given distance, azimuth and elevation with respect to
 185 the instrument, or a uniform emission map of given radiance.

186 **3.1.3 Natural background**

187 In the following, the *natural background* light designates any source of light from the
 188 sky that we approximate as constant and isotropic. It includes two main contributions: the
 189 nightglow (Leinert et al., 1998) and the integrated starlight (e.g. Staude, 1975). The nightglow
 190 is specific as it is well defined in wavelengths (see Table 2). Its emissions can change with time
 191 and it can be highly structured. All-sky camera images, which are unfortunately not available
 192 in the present study, could be used to model the nightglow more precisely. The integrated
 193 starlight covers a wide spectrum over all observed wavelengths and is unpolarized. It varies
 194 with the time and place and could be recovered with astronomical tools in up-coming studies.

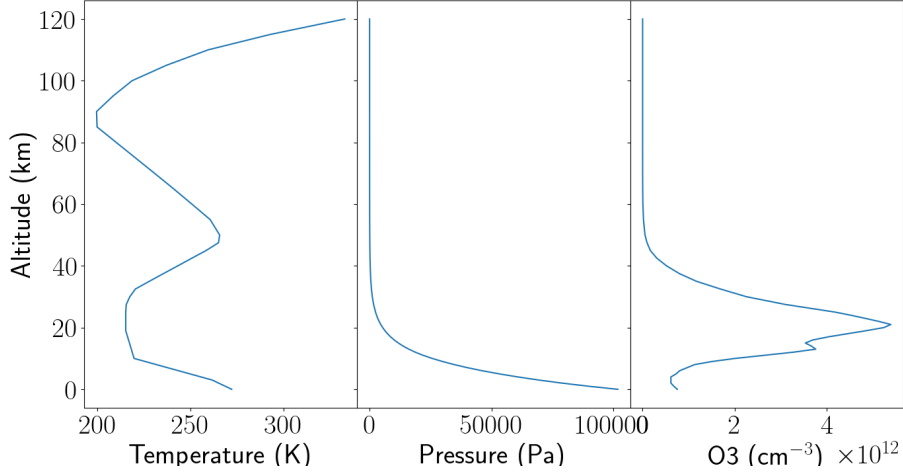


Figure 1: Mid-Latitude night time atmospheric profiles from the 2001 MIPAS model (see text for details). From left to right: temperature [K], pressure [Pa], Ozone number density [cm^{-3}].

195
196
197
198
199
200

For now on, since the absolute values of these contributions cannot be estimated, and also because the absolute radiant flux measured by the instrument is not calibrated, we cannot disentangle the several background contributions from the confrontation of our measurements with the model outputs. Thus, the background contribution may be considered to account for the model uncertainties. These are different for each wavelengths, time and location of observation.

201

3.1.4 Atmospheric properties

202
203
204
205
206

To compute the Rayleigh scattering in the atmosphere, we need different atmospheric parameters. We use the 2001 MIPAS Model Atmospheres (Remedios et al., 2007) up to the lower thermosphere, at 120 km of altitude. It provides the temperature $T(z)$ and pressure $P(z)$ vertical profiles (z is the altitude) as well as an ozone vertical profile. For the present purpose, we use their standard night-time mid-latitude profiles, displayed in Figure 1.

207
208
209
210
211
212
213

To account for the influence of the aerosols, we consider a Lorenz-Mie scattering model (Lorenz, 1890; Mie, 1908; Born & Wolf, 1999; van de Hulst, 1981). This implies a wide range of input parameters, such as the complex refractive index, the aerosol sizes and their vertical profiles. Three aerosol models are considered in this paper, named 1-low, 2-high and 3-mid, whose parameters are listed in Table 1. We use complex optical indices from Dubovik et al. (2000) assumed to be the same for all wavelengths considered in this paper. The size distribution $n(\ln(r))$ of the aerosol is supposed to be log-normal,

$$n(\ln(r)) = \frac{dN}{d\ln(r)} = \frac{N}{\sqrt{2\pi}\ln(\sigma)} \exp\left(-\frac{\ln^2(r/R)}{2\ln^2(\sigma)}\right), \quad (6)$$

215
216
217

with r the aerosol radius (in μm), N the total number of aerosols, R the mode radius (the radius where the distribution is maximal) and $\ln(\sigma)$ controls the dispersion of the aerosol sizes around R . The vertical number density distribution of aerosol $n(z)$ is given by

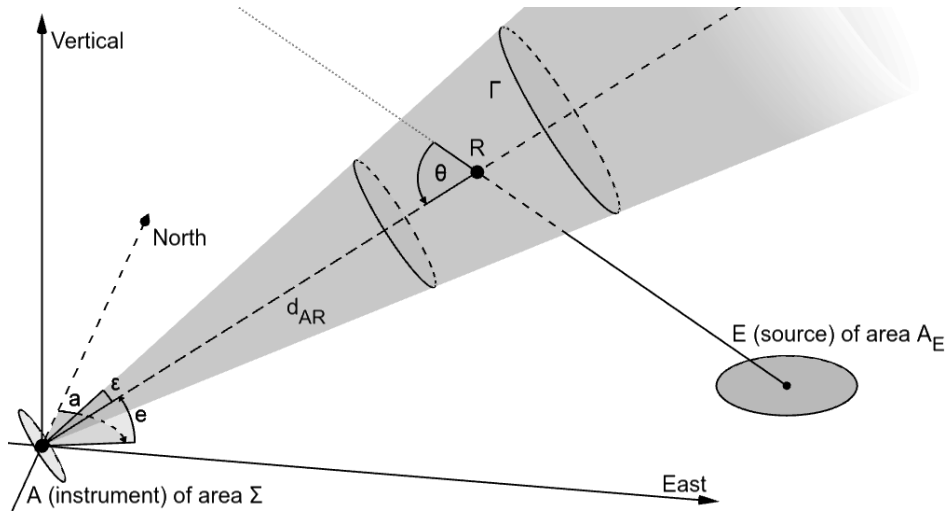
$$n(z) = n_0 \left[\exp\left(\frac{-z}{H}\right) + \left(\frac{n_B}{n_0}\right) \right], \quad (7)$$

219
220

with n_0 the number density at the surface (in cm^{-3}), n_B the minimum number density when z tends to infinity (in cm^{-3}) and H the scale height (in m). The values chosen for the above

Aerosol profile name	Complex refractive index		Size distribution		Vertical number density profile		
	Real	Imaginary	R (μm)	$\ln(\sigma)$	H (m)	n_0 (cm^{-3})	n_B (cm^{-3})
1-low	1.45	0.0035	0.15	0.29	440	4000	10
2-high 3-mid	1.61	0.03	0.557	0.266	500	$\frac{1000}{500}$	1

Table 1: Parameters used to define the aerosol model (see text for details).

Figure 2: Geometry of the problem for a light source in E of area A_E , a scattering volume (Γ) centered at R and the instrument in A of area Σ and half aperture angle ϵ . The instrument pointing direction is defined by its azimuth a and elevation e . θ is the scattering angle.

221 parameters are taken from Jaenicke (1993). In the context of the present paper, we consider
 222 these standard aerosol profiles to be sufficient in order to illustrate our purpose. However, in
 223 future studies they could be recovered from independent measurements (e.g. LIDAR) or using
 224 an inversion scheme in order to best fit polarization data.

225 3.1.5 Topographic map

226 Our model also incorporates the topography around the instrument. It is used for the
 227 computation of occultation: when a light beam hits the ground between the emission and
 228 the scattering point, its contribution to the light received by the instrument is set to zero. The
 229 topographic altitude data are taken from ALOS GLocal Digital Surface Model AW3D30 DSM
 230 of the Japan Aerospace Exploration Agency (Tadono et al., 2016). It has a resolution of 30 m,
 231 which can be downgraded in order to reduce the computation time.

232

3.2 One-dimensional radiative transfer model

233

3.2.1 Computations for a single point source over a single scattering volume

234

In a first step, we describe the properties of the light (at a given wavelength) reaching our modeled instrument located at point A (hereafter called *virtual instrument*), coming from a single emission point source E , and scattered at a single point R along the line of sight (see Figure 2).

238

In this scenario, we shortly discuss here the computation of the radiant flux F_A measured by the instrument, as well as the *DoLP* and *AoLP* of the light scattered towards it.

240

Firstly, the radiant flux F_A measured by the virtual instrument depends on many physical quantities described in detail in Appendix A. It takes into account Rayleigh and Lorenz-Mie scattering, the atmospheric model via particle concentration and phase function, the optical extinction along the path, as well as the general geometry of the problem.

242

Secondly, the *DoLP* of a light beam scattered at an angle θ via Rayleigh scattering is (McFarlane, 1974)

246

$$DoLP^{ray}(\theta) = \frac{\sin^2 \theta}{1 + \cos^2 \theta}. \quad (8)$$

247

Thirdly, the associated *AoLP*^{ray} is determined by the direction \mathcal{D}^{ray} perpendicular to the plane defined by the incoming (ER) and the scattered (RA) light beams (see Fig. 2). The *DoLP* for the same incoming light beam scattered now by aerosols at the same angle θ , $DoLP^{aer}(\theta)$, is given by the Lorenz-Mie scattering theory. Its direction of polarization \mathcal{D}^{aer} , always perpendicular to the line of sight, is either parallel to \mathcal{D}^{ray} (in which case with our conventions $DoLP^{aer} \in [0, 1]$) or perpendicular to \mathcal{D}^{ray} (i.e. $DoLP^{aer} \in [-1, 0]$).

253

Thus, when the polarized radiant flux along the line of sight from Rayleigh scattering dominates over that from Lorenz-Mie scattering ($F_A^{ray} DoLP^{ray}(\theta) \geq F_A^{aer} |DoLP^{aer}(\theta)|$), following the Rayleigh scattering theory, the measured *AoLP* is $AoLP^{ray}$. In the alternative configuration, the *AoLP* is $AoLP^{aer}$ determined by \mathcal{D}^{aer} , possibly 90° off with respect to $AoLP^{ray}$. In all cases, the *DoLP* for the sum of the Rayleigh and aerosol scattered radiant fluxes is

258

$$DoLP(\theta) = \frac{|F_A^{ray} DoLP^{ray}(\theta) + F_A^{aer} DoLP^{aer}(\theta)|}{F_A}. \quad (9)$$

259

$DoLP(\theta)$ is always taken as positive. The sign of $DoLP^{aer}$ gives information on the direction of polarization of the light. This is not useful here because the direction of polarization is given by the *AoLP* in the following work. To keep consistency with the real instrument, we set the zero of the *AoLP* along the vertical direction, and thus $AoLP = \pm 90^\circ$ in the horizontal direction, when the virtual instrument points horizontally. The *AoLP* is positive in the trigonometric direction (anti-clockwise) when looking towards the source. The *AoLP* is π periodic, such that we define it in the interval $[-90^\circ, 90^\circ]$.

266

3.2.2 Integration over all sources and along the entire line of sight

267

Once the light polarization characteristics for a single path are computed (the radiant flux F using equation A17, the *DoLP* and the *AoLP* using equation 9), the model repeats this computation for every point R along the line of sight and every point source E given in input. We then integrate along the line of sight and over all point sources by summing all these contributions. However, this integration is not straightforward, since the *DoLP* and *AoLP* are not linear quantities. For example, the resulting *DoLP* from the mix of two light rays with different *DoLPs* is not their average if the *AoLPs* are different. In order to maintain the same formalism between the virtual and the real instruments, we use the Stokes parameters in spherical coordinates (McMaster, 1954; van de Hulst, 1981), which are equivalent to equation

275

276 (4):

$$\begin{aligned}
 277 \quad I &= \frac{F}{2}, \\
 278 \quad Q &= \frac{F \text{ DoLP}}{4} \cos(2 \text{ AoLP}), \\
 279 \quad U &= \frac{F \text{ DoLP}}{4} \sin(2 \text{ AoLP}).
 \end{aligned}
 \tag{10}$$

281 When integrating over the line of sight (*l.o.s.*) and over all the sources given in input, we can
 282 add up the Stokes parameter and get back to the resulting *DoLP* and *AoLP* via the relations
 283 given in equation (5). In the end, the final polarisation parameters are:

$$\begin{aligned}
 284 \quad I^{total} &= \sum_{sources} \sum_{l.o.s.} I, \\
 285 \quad Q^{total} &= \sum_{sources} \sum_{l.o.s.} Q, \\
 286 \quad U^{total} &= \sum_{sources} \sum_{l.o.s.} U.
 \end{aligned}
 \tag{11}$$

288 4 Model validation and influence of the parameters

289 In this section we study:

- 290 i) The influence of a localized source on the ground (such as a cities), at several distances
 291 from the instrument, and in the absence of any source in the sky ;
- 292 ii) The influence of the atmospheric parameters (absorption by O_3 , aerosols) for a local-
 293 ized source on the ground;
- 294 iii) The effect of a uniform source in the sky, polarized or not, in the absence of any source
 295 on the ground.
- 296 iv) The domain of validity of the single scattering approximation (in comparison with mul-
 297 tiple scattering) by comparing POMEROL outputs with modeling and observations
 298 provided by Pust & Shaw (2011).

299 These reduced configurations have been chosen so as to illustrate the most important factors
 300 that impact ground-based polarization measurements. In the following, we present results by
 301 means of clockwise almucantars of elevation 45° , the starting direction being the North. The
 302 virtual instrument parameters (Σ and ε) correspond to that of the real polarimeter (see Section
 303 3.1.1). We show here results at $\lambda = 557.7$ nm (auroral green line, Table 2). In the following
 304 series of tests, we use a polarized Lorenz-Mie scattering model for scattering by aerosols (see
 305 Section 3.1.4). The comparison between the aerosols models and real data is shown later on
 306 in Section 5.1.2. The atmospheric profile used for the tests is the MIPAS standard night-time
 307 mid-latitude profile (see Section 3.1).

308 4.1 Influence of a localized source on the ground in absence of any source in the sky.

309 We consider an isotropic point source on the ground of radiance $100 \text{ nW/m}^2/\text{sr}$, at dif-
 310 ferent distances d_{AE} away South of the virtual instrument. The purpose of this arbitrary setup
 311 is only to showcase the influence of a point source on the ground at different distances from
 312 the instrument. Thus, the radiance is arbitrary and the distances are chosen to be representa-
 313 tive of a real environment (between 1 and 100 km). There is no mountain obstruction. The
 314 ground surface takes the Earth curvature into account. Only Rayleigh scattering and ozone
 315 absorption are taken into account, no aerosols are present in the atmosphere. The ozone is
 316 taken into account through its number density vertical profile (Figure 1) and its absorption
 317 cross sections as a function of the wavelength (Figure A1). For a source located 100 km away
 318 from the observation point, the ozone decreases the measured radiant flux by less than 3%.
 319 There is no effect on the *AoLP* since this angle depends only on the scattering plane (defined

by the emission and scattering direction). The effect on the *DoLP* is smaller than 0.4%, and the closer the source, the lower the effects. More complex sources than a point may slightly increase these values. From now on, we take into account the impact of O_3 .

In Figure 3, we show the polarization results for $d_{AE} = 1, 5, 10, 50$ and 100 km. In all such figures, the upper panel shows the radiant flux measured by the virtual instrument, representing the energy per unit time on the collector, the middle panel shows the *DoLP* and the lower panel the *AoLP*.

The further the source, the lower the measured radiant flux. However, the effect is not merely a decrease as $1/\sqrt{d_{AE}}$, because the source illuminates points at all altitudes along the line of sight that are integrated on the virtual instrument. Moreover, the light parameters change during its crossing into the atmosphere from the source to the line of sight, and along the line of sight. As seen in Figure 1, the concentration in ozone peaks at about 20 km. As an example, the decreasing factor between a source lying at 1 and 10 km is about 25 (and not 10^2 if only the effects of the distance were considered). It becomes approximately 5 000 (and not 10^4) with a source at 100 km compared to 1 km. Because of the exponential decrease of the atmospheric pressure with the altitude, this effect is less important when the source moves away from the polarimeter. However, in all cases, the radiant flux is maximum in the Southern direction, i.e. toward the source.

Geometrically, for a single point source and a given line of sight, the *AoLP* of every scattering point is the same. In this particular case, we do not have to use the I , Q and U notation (equations 11). The total *DoLP* integrated along the line of sight is an average of the *DoLP*(θ_i) of each scattering points i weighted by the scattered radiant flux F_i as

$$DoLP = \frac{\sum_i F_i DoLP_i(\theta_i)}{\sum_i F_i}, \quad (12)$$

where θ_i is the scattering angle at point i , F_i follows equations (A17) and $DoLP_i$ equation (9). In the limit of a source infinitely far away from the instrument (on a flat surface), all paths from the source to the instrument are parallel. Thus, the scattering angle is the same everywhere on a given line of sight. The total *DoLP* measured by the virtual instrument should then follow equation (8) (dashed line in Figure 3, middle) since there is no aerosols in this case. When looking eastwards and westwards, the value of the *DoLP* reaches 100% as expected from the theory. When the source gets closer to the virtual instrument, each point along the line of sight has a different scattering angle, which smooths the variations along the almucantar. On a flat surface, the *AoLP* is the same whatever the distance from the source (Figure 3, bottom).

4.2 Influence of the aerosols for a localized source on the ground

The aerosols are taken into account through their number density vertical profiles and their cross sections (Table 1). The aerosol cross section depends on the wavelength as computed using Lorenz-Mie theory (Lorenz, 1890; Mie, 1908; Born & Wolf, 1999). For the sake of simplicity, we consider the aerosol refractive index to be the same for all wavelengths. A variation of the refractive index with wavelength could be taken into account, but is out of the scope of the present study.

In order to illustrate the effect of the aerosols, we consider three different profiles listed in Table 1: 1-low, 2-high, 3-mid. The impact of the aerosol profiles is drastic, but not straightforward to interpret. It is illustrated in Figure 4, for a point source located 5 km South from the observation point. With the 1-low model (lowest aerosol contribution), the radiant flux is increased by 600% (with respect to the case with no aerosols) when pointing above the source, and by 40% in the opposite direction. Using the 2-high profile (highest aerosols contribution), the radiant flux is increased by 150% when pointing above the source, and decreased by 40% in the opposite direction. With the 2-mid model, the radiant flux above the source increases by 120%, against 10% in the opposite direction. The ratio of the maximum to minimum radiant flux along the almucantar is in all cases amplified by the presence of aerosols.

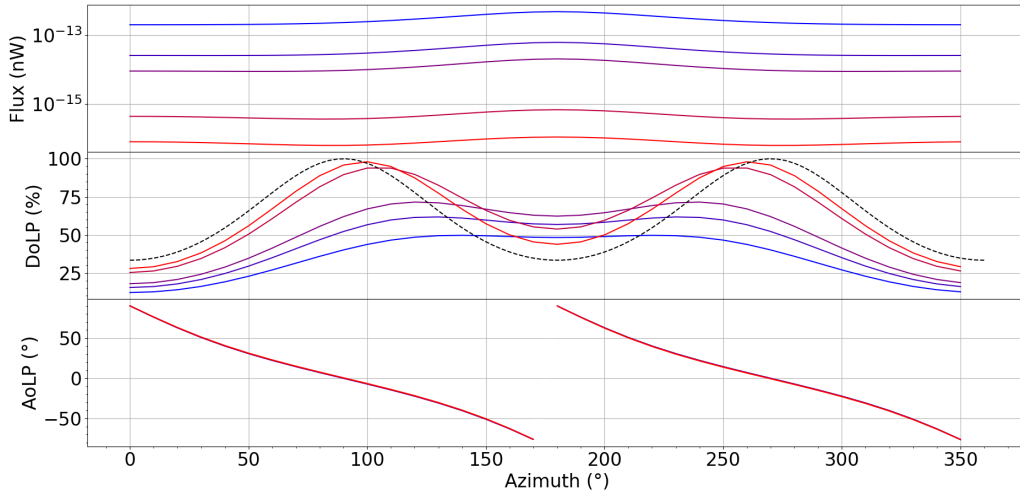


Figure 3: Almucentar for $e = 45^\circ$, for a point source on ground, on a flat Earth surface, South of the instrument at varying distances d_{AE} (with no aerosols). Upper panel: measured radiant flux [nW] for a source of radiance $100 \text{ nW/m}^2/\text{sr}$. Middle panel : DoLP [%]. Lower panel: AoLP [$^\circ$]. From blue to red: $d_{AE} = 1, 5, 10, 50, 100$ km. In the upper panel, the highest value (in blue) corresponds to the closest source position and the lowest value (in red) to the most distant point source. Similarly, in the middle panel, the most distant point source has two very marked maxima (in red) while the closest is the flattest (in blue). The dashed line in the middle panel corresponds to a theoretical case for a source at infinite distance.

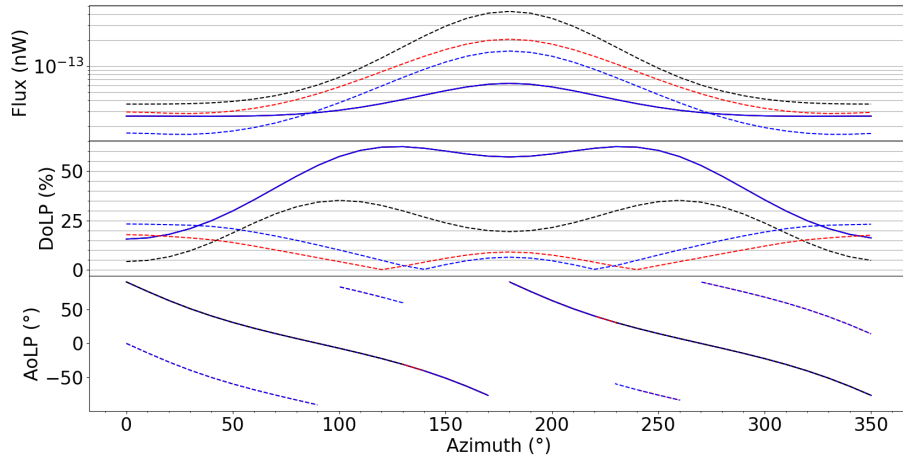


Figure 4: Almucentar for $e = 45^\circ$, for different aerosol profiles. A point source is located 5 km South of the instrument. The continuous line is the case without aerosols (similar to Figure 3). The dashed lines correspond to three different aerosol models listed in Table 1: 1-low (black), 2-high (blue) and 3-mid (red).

364 For an increasing aerosol contribution, the *DoLP* decreases in the direction of the source.
 365 With the 1-low model, it decreases by about 50%, with the two maxima along the almucantar
 366 still present. The *AoLP* does not change since the aerosol radius is small compared to the
 367 wavelength, and the polarization direction is the same as for Rayleigh scattering (*AoLP^{ray}*).
 368 However, when the aerosol size is large compared to the wavelength (2-high and 3-mid), the
 369 *DoLP* behavior changes drastically, with a maximum at about 25% when pointing away from
 370 the source. The *AoLP* is shifted by 90° when pointing away from the source due to larger
 371 aerosol size, while it is the same as *AoLP^{ray}* when pointing towards the source. The impact
 372 of aerosols on the virtual instrument observations is complex. They may for instance either
 373 increase or decrease the intensity depending on their size or on the scattering angle. They do
 374 therefore play a major role. Spanning all possible aerosol models is not a crucial point for this
 375 study, and we limit ourselves to the three models presented here.

376 4.3 Influence of the skylight with different polarization parameters

377 We document here the effect of a simple skylight (nightglow and/or integrated star light).
 378 It is modeled as an infinitely thin uniform sky emission of arbitrary intensity at 110 km of
 379 altitude. The model computes the sum of the non scattered light and the single Rayleigh
 380 scattered light measured by the instrument. In order to prepare for further auroral studies (out
 381 of the scope of this article), we allow this emission to be polarized (Bommier et al., 2011).
 382 Figure 5 shows the model outputs over an almucantar (with no aerosols), for a nightglow
 383 either unpolarized, or polarized with a $DoLP = p_{source} = 1\%$ (arbitrary choice) along several
 384 directions: East-West (EW), North-South (NS) or along the magnetic field (B). For this last
 385 case, the instrument is positioned at latitude 45.2123°N and longitude 5.9369°E and we use
 386 the CHAOS-6 internal magnetic field model (Finlay et al., 2016) evaluated in 2019. The
 387 atmospheric profile described in Section 3.1 is used. As the background skylight is isotropic,
 388 the measured radiant flux does not change over an almucantar.

389 In cases where the nightglow is polarized, the *DoLP* depends on the angle α between
 390 the line of sight and the polarization direction, as $DoLP = p_0 + p_1 \sin \alpha$. For the EW and
 391 NS cases, $p_0 \approx 0.85p_{source}$ and $p_1 \approx 0.1p_{source}$. When the nightglow is polarized along the
 392 magnetic field lines, the behaviour is much different as the lines are close to vertical, with
 393 $p_0 \approx 0.6p_{source}$ and $p_1 \approx 0.3p_{source}$. For a uniform sky emission and in the absence of other
 394 sources, Figure 5 shows that the polarization from Rayleigh scattering in the atmosphere is
 395 relatively small compared to the polarization of the non scattered light. Thus, in this simple
 396 configuration, any polarized source in the sky with a *DoLP* higher than the instrument noise
 397 level should be detectable.

398 The *AoLP* (lower panel) for the unpolarized nightglow emission (continuous black line)
 399 is undefined (it is set to zero by default, with no physical meaning). The EW and NS cases
 400 show an *AoLP* regularly rotating over all 360° with the same behavior, but shifted in azimuth
 401 by 90° . As expected from the *DoLP* definition, the maximum *DoLP* corresponds to a 90°
 402 *AoLP*. When the nightglow polarization direction is aligned along the magnetic field, the
 403 magnitude of the *AoLP* variations along an almucantar is significantly weaker, within $\pm 40^\circ$,
 404 which led Bosse et al. (2020) to reject this single source as the origin of the measured polar-
 405 ization of auroral lights.

406 4.4 On the impact of multiple scattering

407 The model described here does not consider the effects of multiple scattering. We recall
 408 that the main goal of this approach is to test the feasibility of night-time polarisation mea-
 409 surements and modelisation, and not to develop a new state of the art radiative transfer code.
 410 However, these effects can not be neglected, in particular at the shortest wavelengths, and we
 411 document here their impact. The literature on the atmospheric polarization is already large,
 412 both in term of observation and modeling. The reader may refer to the seminal work of Hoven-
 413 nier (1971) and Hansen & Hovenier (1971) on the modelisation of terrestrial and planetary

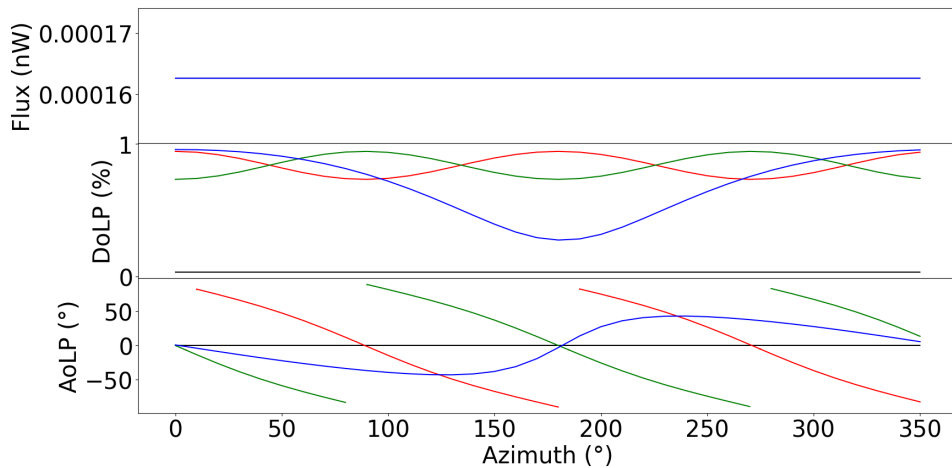


Figure 5: Polarization parameters for an almucantar at $e = 45^\circ$ in the presence of an isotropic skylight of radiance taken at $100 \text{ nW/m}^2/\text{sr}$ at 557.7 nm . No aerosols are present in the model. The direct radiant flux is taken into account, with different polarization parameters. No polarization of the skylights (black line), with a 1% polarization along the East-West (red) and North-South (green) directions, and along the magnetic field direction (blue).

414 clouds enlightened by the sun. It is known that single scattering models of the atmosphere miss
 415 part of the measured polarization properties, especially at short wavelengths. The limitations
 416 of the single scattering approach was for instance addressed by Hansen & Travis (1974) who
 417 showed the early improvements brought by multiple scattering (MS). Polarization properties
 418 are not erased by MS (Hansen, 1971). Generally, in comparison with single scattering, MS
 419 tends to enhance the radiant flux and reduce the *DoLP*, with relative effects that depend on the
 420 optical depth, the solar elevation and the wavelength (Hovenier, 1971). An order of magnitude
 421 of the MS effect is proposed for instance by Staude (1975) who mentioned an increase in the
 422 radiant flux ranging from 10 to 45%, and a drop in the *DoLP* from 5 to 20%, depending on the
 423 optical depth. It is acknowledged that simply using a scaling factor to accurately match *DoLP*
 424 and radiant flux observations with single scattering is over-simplistic (Hansen & Hovenier,
 425 1971). In atmospheric optics, the SSA is more of an issue towards short wavelengths (e.g.
 426 Hovenier, 1971), while it can give decent predictions for red and longer wavelengths. There
 427 are several approaches to polarized MS, such as adding-doubling methods with several levels
 428 of refinement, Monte-Carlo methods, etc. (de Haan et al., 1987; King, 1986; Ramella-Roman
 429 et al., 2005). For a review of multiple scattering of waves from the theoretical perspective, see
 430 for example Lax (1951).

431 Several studies addressed the comparison between single and multiple scattering of po-
 432 larized light in the atmosphere. One can cite Evans & Stephens (1991), but also a series of
 433 balloon experiments (Herman et al., 1986; Santer et al., 1988), which interpretation was first
 434 based on a single scattering approach, and later on refined with MS. Ugolnikov & Maslov
 435 (2002), followed by Ugolnikov et al. (2004) proposed a thorough study on the impact of MS as
 436 a function of the wavelength in the visible range. They conclude to a radiant flux contribution
 437 from single scattering ranging from about 55% in the blue to over 80% in the red (slightly
 438 less than theoretical estimates). A comprehensive study over a wide range of wavelengths
 439 and zenith angles can also be found in Pust & Shaw (2011) (mentioned as PS11 hereafter), in
 440 various aerosols conditions.

441 However, the configuration of our experiment significantly differs with most of the al-
 442 ready documented work. PS11 for instance evaluate the polarization of the solar light scattered
 443 in the atmosphere. They do not study the *AoLP*, and only provide measurements of the max-
 444 imum *DoLP*, i.e. in a direction at approximately 90° from the Sun direction. Many of such
 445 studies also consider the rising Sun only. In our case, we consider a mixture of sources, either
 446 extended or localised, during the night-time, and observed over a multiplicity of angles.

447 Then, because our study constitutes a first approach to a fully new principle of night-
 448 time atmospheric observations, we wish to keep our set-up as simple as possible, although
 449 realistic, and we do not account for MS in this prototype version of the POMEROL model. Its
 450 effect is out of the scope of the present work, and should constitute a dedicated future study.
 451 As we will see later, already a large part of our night-time measurements can be interpreted in
 452 the single scattering approximation, which means that the SSA an already catch a great part of
 453 the phenomenon we are dealing with. This is particularly true not only for the *DoLP* profiles
 454 along one almucantar, but also for the *AoLP* data, a quantity that is almost never considered
 455 in the literature. Meanwhile, we provide below an estimate of the uncertainty level associated
 456 with this limitation of our model, by presenting comparisons of POMEROL with previously
 457 published observations and MS model predictions from PS11.

458 These authors studied the output of the MODTRAN-P model (e.g. Berk et al., 2014),
 459 accounting or not for the effect of MS. Their model was tested against measurements cor-
 460 responding to various aerosol contents: a clear day with low aerosol content, another day
 461 following a forest fire with high aerosol content and finally shortly after the fire, a day with
 462 moderate aerosol content. For each day, they measured the *DoLP* of the sky with an all-sky
 463 camera at different wavelengths, and compared the maximum *DoLP* found in the sky with
 464 their model prediction, as a function of solar elevation. They found that single scattering over-
 465 estimates the *DoLP*, while it is under-predicted by unpolarized MS. However, in low aerosol
 466 conditions, the SSA is sufficient to reproduce their data for long wavelength (> 630 nm).

467 We report their measurements in Figure 6 at three representative wavelengths (630, 530
 468 and 450 nm) and for the two extreme days with low and high aerosol content. We see a de-
 469 crease of the maximum *DoLP* with increasing solar elevation. This effect is more important
 470 for high aerosols conditions and stronger for large elevations and short wavelengths. To re-
 471 produce the above configuration with POMEROL, we set a point source at a given elevation
 472 representing the Sun, and compute the *DoLP* for each observation direction in the sky. We
 473 then take the maximum *DoLP*, which is always found in a direction around 90° of the Sun for
 474 low aerosol contents. No ground reflections are taken into account. We use the 1-low aerosol
 475 profile for the day before the fire, and the 2-high aerosol profile for the time just after the
 476 fire. Note that the vertical concentration profiles have been tweaked so that the optical depth
 477 matches that of the aerosol profiles considered by PS11.

478 In the first case with low aerosol content, POMEROL overestimates the maximum *DoLP*
 479 for short wavelengths: at 450 nm, the modeled *DoLP* is $\sim 20\%$ too high (in relative values).
 480 At 630 nm however, single scattering predictions from POMEROL are much closer to the
 481 observations, although our model does not reproduce the $\sim 10\%$ relative increase seen in the
 482 maximum *DoLP* for low elevation angles. This result is overall consistent with the behavior
 483 of MODTRAN-P by PS11 in similar conditions: single scattering model with a low aerosol
 484 content (see Figure 7). The several low aerosol models considered by PS11 give a hint of the
 485 sensitivity to this parameter, with a spread of the predicted maximum *DoLP* that ranges from
 486 5% to 8% from 450 to 630 nm (i.e. less than $\sim 10\%$ in relative values).

487 In the case with high aerosol content the observed maximum *DoLP* decreases from
 488 around 45% at low solar elevation down to $\sim 30\%$ at 630 nm and it decreases from 35% to
 489 15% at 450 nm for solar elevation above 20° . This trend is overall recovered with POMEROL
 490 that shows a net decrease in the *DoLP* at solar elevation above 20° in all wavelength (see
 491 Figure 6). At 450 nm, the maximum *DoLP* is well reproduced at high and low solar elevation,
 492 but is overestimated in between. At 630 nm and 530 nm, the *DoLP* is overestimated for all

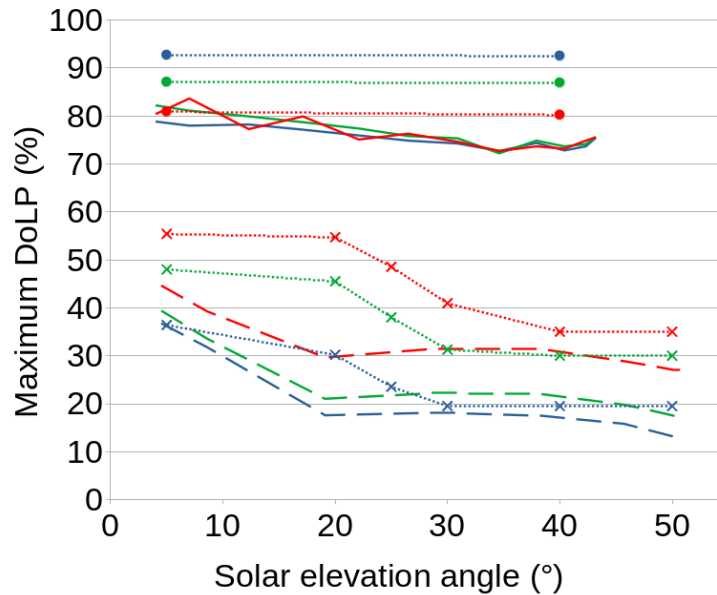


Figure 6: Maximum *DoLP* found over the sky as a function of solar elevation angle at three wavelengths: 630 nm (red), 530 nm (green) and 450 nm (blue). Observations from PS11 are shown in plain lines (resp. dashed lines) for a low (resp. high) aerosols content. Predictions from POMEROL are shown in dotted lines with circled (resp. crosses) for low (resp. high) aerosols content.

493 angles, with larger differences around 20° solar elevation. In comparison, the single-scattering
 494 model predictions by PS11 overestimate the maximum *DoLP* by a factor as large as ~ 2
 495 at 450 nm (see Figure 7). Here again the difference with our model might come from distinct
 496 aerosol profiles used in both studies.

497 As shown with the above example, POMEROL tends to overestimate the *DoLP* for a
 498 day-like environment, i.e. a single point source at infinity. This effect is sensitive to the aerosol
 499 profile, the wavelength and whether or not MS is considered in PS11. The benefits that we
 500 could gain by implementing MS is expected to be larger at short wavelengths. Meanwhile,
 501 we notice that the above test situation differs from our experimental environment in several
 502 ways. During the day, the Sun is approximated as a single point source because it dominates
 503 other light sources. By night on the contrary, light pollution from urban lightning and spread
 504 emissions from the integrated star light and airglow are mixed all together. In this case, the
 505 measured polarization depends heavily on the relative contributions of the different sources
 506 rather than on the absolute contribution of each one. We thus expect MS impact on the *DoLP*
 507 and *AoLP* to decrease for night-time scenarios.

508 MS can not be neglected in most cases, particularly at short wavelengths ($\approx < 600$ nm).
 509 The conditions of our experiment corresponds to a low aerosol content. In this case, only a
 510 moderate sensitivity to the source angle has been reported, and we can expect MS to decrease
 511 the *DoLP* by at most about 20% at 450 nm, and less for longer wavelengths. MS is thus
 512 expected to result in a more isotropic contribution than single scattering, with a lower *DoLP*.
 513 For the sake of simplicity, we then incorporate its effect together with that of the uniform,
 514 isotropic and unpolarized emission in the sky (both tend to reduce the *DoLP* and increase
 515 the radiant flux). One consequence of this coarse approximation is that we cannot isolate
 516 unambiguously the signature of the airglow and/or starlights. Still, this parsimonious approach

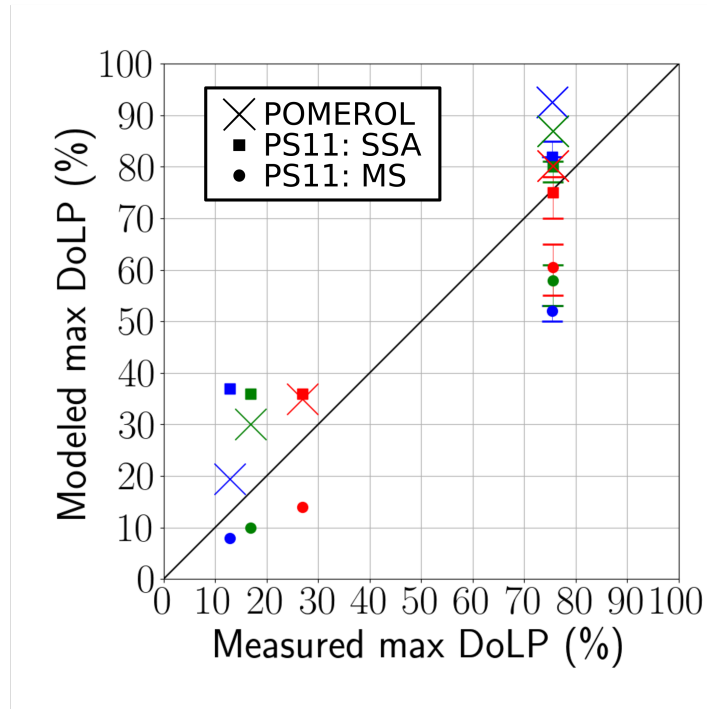


Figure 7: Comparison of POMEROL and MODTRAN-P maximum *DoLP* with the PS11 observations at maximum solar elevation, at three wavelengths: 630 nm (red), 530 nm (green) and 450 nm (blue). The group of points with *DoLP* < 40% correspond to a high aerosol content, while symbols in the upper right quadrant correspond to a low aerosol content. Crosses represent the result of POMEROL. Single (resp. multiple) scattering predictions obtained with MODTRAN-P by PS11 are indicated with squares (resp. circles). The spread within the several low aerosol contents investigated by the authors is indicated by errorbars.

Name	Wavelength (nm)	Instrumental width (nm)	Atmospheric source	Layer
Orange	620	2	OH	High Mesosphere (< 80 km)
Green	557.7	10	O	Thermosphere (110 km)
Blue	427.8	10	N_2^+	Ionosphere (90 km)
Turquoise	413	10	O_2	Mesosphere (< 80 km)
Purple	391.4	10	N_2^+	Ionosphere (85 km)

Table 2: List of emission lines observed during the January, 2021 campaign (see text). All emissions are present in the light pollution spectrum.

517 appears to be enough to account for a significant part of our observations for wavelengths down
518 to the blue line at 427.8 nm, as we shall see later.

519 5 Comparison with geophysical measurements at mid-latitude

520 In order to validate our model, we performed a series of observations in the French Alps.
521 In the following, we focus on the night from 19 to 20 January, 2021 when the moon was down
522 (below -10° elevation during the whole observation). The latitude is 45.2123° and longitude
523 5.9369° . The altitude is 770 m. The nearest city is Grenoble 15 km away with downtown
524 at an azimuth of 260° . However, the valleys around this bright city produce also some light
525 pollution. Figure 8 shows the geographical configuration with lines of constant elevation at
526 500 m, 1000 m and 2000 m.

527 The light pollution was clearly visible with the naked eyes. At the time of the observa-
528 tions, the snow was covering the ground above about 500 m elevation. The altitudes below
529 $h \approx 1500$ m are mostly covered with forests in the mountains which lowers the albedo signif-
530 icantly, even though some snow remains on the trees. The air temperature was below 0°C all
531 over the surrounding area, and reached about -5°C at the point of observation. The modeling
532 below takes the relief into account (see Section 3.1). We could observe simultaneously five
533 wavelengths, summarized in Table 2: three of them concern emissions bands emitted in the
534 upper atmosphere, either in the thermosphere (green, due to the O^{1S} excitation state) or in the
535 thermosphere (blue and purple, due to the $1^{st} N_2^+$ negative band). The "orange" band around
536 620 nm is not present in the thermosphere, but is emitted in the mesosphere by OH(5-0) and
537 OH(9-3), though with a relatively lower radiant flux (Broadfoot & Kendall, 1968; Bellisario
538 et al., 2014, 2020). Finally, the turquoise line can be produced by Herzberg and Chamberlain
539 O_2 lines and/or ground light pollution. The former indeed induce spectral lines of weak inten-
540 sity (Broadfoot & Kendall, 1968; Leinert et al., 1998), while the latter, which we account for,
541 might be related to the presence of Hg in city lights. The two contribution are likely weak,
542 and the main Hg line falls outside the filter bandwidth.

543 We show below the results of an almucantar at a constant elevation $e = 45^\circ$ from 1:18
544 UT to 3:35 UT taken with the real instruments and compared to the virtual one (i.e. the
545 modeling). We rotate clockwise from North to the East and back to North with 10° increments
546 in azimuth. At each step in azimuth, we record the radiant flux, $DoLP$ and $AoLP$ during about
547 $1'30''$. We recall that our instrument provides the relative (uncalibrated) measurements of the
548 radiant flux, and the calibrated $DoLP$ and $AoLP$. The orientation angles e and a are set using
549 stars as references, together with a compass (to help on the increments in azimuth) and an
550 inclinometer (for the elevation). We consider the accuracy to be of the order of $\pm 2^\circ$.

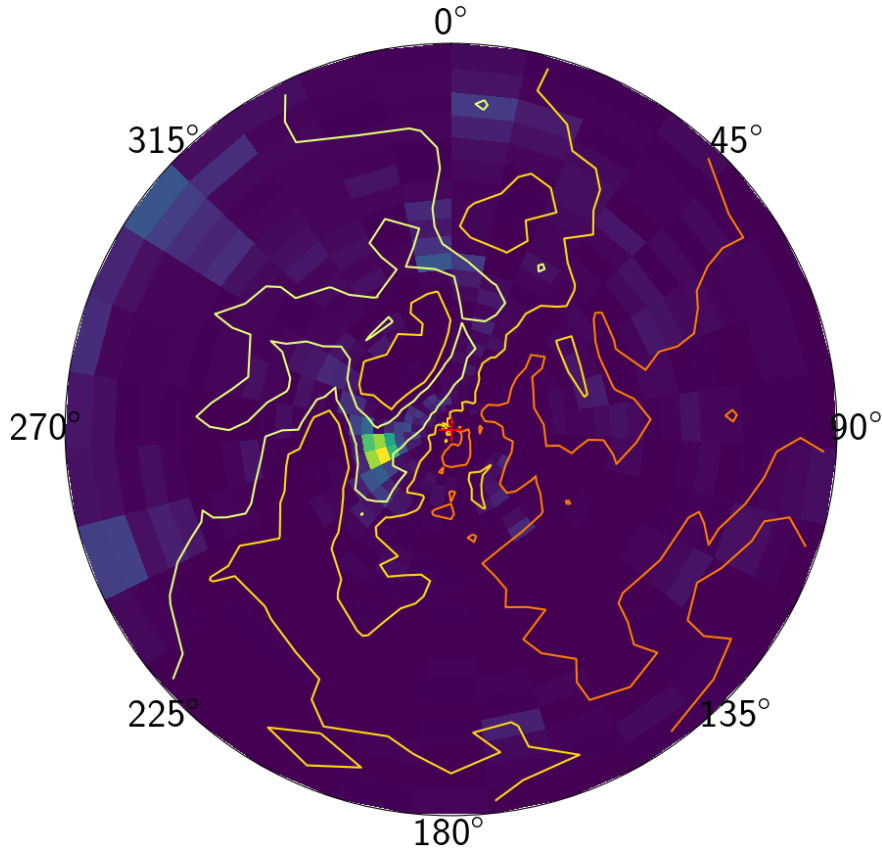


Figure 8: Input emission map and contour of the elevation map for altitudes 500 m (white), 1000 m (yellow) and 2000 m (orange). The instrument is at the center of the map (red cross). Grenoble is the bright emission west to the instrument. The map covers 100 km around the instrument.

551 We focus first on a single wavelength (the green line, see Section 5.1) for which we
 552 detail our analysis of the observations. We next discuss the full picture in Section 5.2.

553 **5.1 Model predictions versus observations in the green line**

554 Figure 9 shows an almucantar in the green line. The radiant flux maximizes above
 555 downtown Grenoble ($a = 260^\circ$, this is clearer in Figure 10). In the theoretical case of a point
 556 source, the *DoLP* maximizes at $\pm 90^\circ$ of the direction of this point (see Section 4 and Figure
 557 3). Here, the *DoLP* shows a single maximum near 240° in azimuth, illustrating the influence
 558 of an extended pollution source. The value of its measured maximum is around 12%. The
 559 *AoLP* rotates regularly with a behaviour very similar to that of a point source on the ground
 560 westward with respect to the instrument.

561 **5.1.1 In the absence of aerosols and background skylight**

562 We first run our POMEROL model with the light pollution as single input (i.e. with
 563 neither aerosol nor natural background skylight). We use a ground emission map composed
 564 of 1000 pixels mapping an area of 100 km radius around the instrument. The elevation map

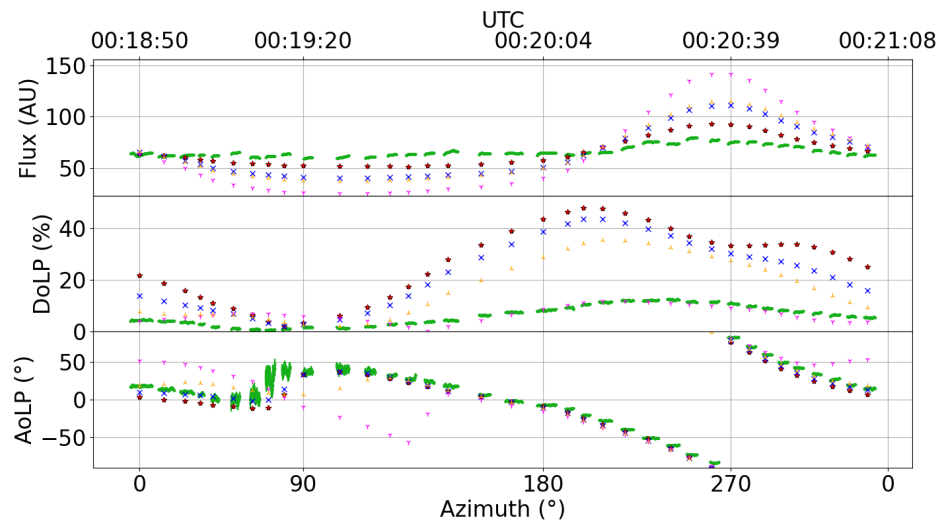


Figure 9: Comparison between model outputs and observational data. Measured data are shown in green, the width of the lines indicating the errorbars (for their computation, we refer to Bosse et al., 2020). Errors on the azimuth due to the pointing direction are of the order of a few degrees (not shown). The other symbols indicate the model output for a ground light pollution map (see text for details). Several aerosol profiles are considered. (see Table 1): without aerosols nor background lights (black \star); without aerosols and with background lights adjusted to fit the radiant flux variations (red $+$); without background lights and with aerosols model 1-low (blue \times), 2-high (magenta ∇) and 3-mid (purple \blacktriangle). Abscissa are given as the pointing direction under the bottom panel (azimuth where 0 is North, 90 is East) and the corresponding time in UTC format above the top panel.

565 covering the same area is used to model the mountain obstructions, with a 30 m resolution.
 566 Note that the emission maps are not intercalibrated with our instrument, so that the units for
 567 the radiant fluxes are arbitrary. The ozone is taken into account, although its effect remains
 568 small. The results are shown in Figure 9 (black stars). Both the modeled and measured radiant
 569 fluxes peak around the same azimuth (260°). However, the radiant flux variations along one
 570 almucantar are significantly larger for the model: the maximum radiant flux is 110% higher
 571 than the minimum for the model, with respect to only 43% for the measurement.

572 The modeled *DoLP* reaches 47% at its maximum around 200° azimuth, about 4 times
 573 higher than the highest measured *DoLP*, and is offset by 40° in azimuth. A second local
 574 maximum at 300° azimuth is also present in the model, and absent from the measurements.
 575 Two maxima in the *DoLP* are indeed expected for a point source (see Figure 3) and are due
 576 to the scattering in the first few kilometers of atmosphere. Here it is smoothed out because of
 577 the multiple light sources and the occultation from the mountains. This feature is not present
 578 in the data and may hint that the model overestimates the scattering below 10 km.

579 The modeled *AoLP* is very similar to the measurement, showing the same rotation pat-
 580 tern at almost the same angles, except around 90° in azimuth (i.e. pointing away from Greno-
 581 ble). This difference can be explained by the poor quality of the data in this direction where
 582 the radiant flux is minimal and the *DoLP* close to zero, inducing large uncertainties on the
 583 *AoLP* measurements (see Bosse et al., 2020).

584 This first simple approach does not take into account one or more additional sources.
 585 We will now show the effects of introducing either a natural background light or the aerosols.

586 **5.1.2 Impacts of aerosols and background skylight**

587 The fact that the model overestimates the radiant flux variations and the *DoLP* in the
 588 case above is an indication that non-polarized (or little-polarized) additional sources must be
 589 taken into account. Such sources exist naturally: they are the nightglow and the integrated
 590 star light. This trend can also be due to the lack of multiple scattering in the model (see
 591 Section 4.4). The exact contributions of these effects is delicate to evaluate at this point, so
 592 we fit them as a whole called a *background skylight* in such a way that the relative variations
 593 of the modeled radiant flux match the measured ones. This method constitutes therefore an
 594 indirect estimate of this background skylight (see red + in Figure 9). Here, it is considered
 595 constant, isotropic and unpolarized (these approximations could be reconsidered in the future
 596 by estimating each contribution from independent measurements or more accurate models, see
 597 Section 3.1.3). Averaged over an almucantar, this results in approximately doubling the total
 598 radiant flux received by the instrument. This is not visible in Figure 9 because of the Arbitrary
 599 Unit radiant flux scale. As expected, the *DoLP* is decreased in any direction by about 50%,
 600 peaking at 25% around 220° in azimuth. The two maxima in the modeled *DoLP* over one
 601 almucantar are still present, although the secondary maximum appears attenuated. The *AoLP*
 602 is unchanged in comparison with the previous case with no background sky, which is expected
 603 since the natural background is not polarized.

604 We now turn to a case with no background skylight, but with the aerosol polarized
 605 models included (see Section 3.1.4). The amplitude of the modeled radiant flux variation
 606 along the almucantar become larger, whatever the aerosol model, as seen with the synthetic
 607 case in Figure 4. The higher the aerosol contribution, the higher the radiant flux variations.
 608 The modeled *DoLP* decreases when the aerosol contribution increases, so that it is possible to
 609 find a model (2-high: magenta λ) that matches the measured *DoLP*. However, this makes the
 610 modeled *AoLP* depart from the measurements, so that it is not possible to find a set of aerosol
 611 parameters that allows fitting the measured radiant flux, *AoLP* and *DoLP* at once.

5.2 Comparison of the observations and the modeling in five wavelengths.

From the results presented above, we deduce that even though both additional sources (background and aerosols) significantly affect the polarization parameters, none of them reproduce the measurements alone. We consider below the model predictions for a combination of those two contributions. We first have to choose an aerosol profile. We use the 1-low aerosol model, as it fits best the measurements when combining with background skylight. It could already be intuited from Figure 9 as the 1-low profile affects less the *AoLP* than the other ones. This choice is also coherent as we observe in the Alps at an altitude where the air is very clean. We show hereafter model outputs with this aerosol profile together with a natural background skylight. At all wavelengths, the modeled radiant flux is the highest in the direction of the city of Grenoble, and the model predictions for the *AoLP* convincingly fit the observed values (see Figures 10 to 14).

The magnitude of the signal from the ground is likely very small in the purple (391.4 nm) and turquoise (413 nm), because in these wavelengths the radiant flux of city lights is in average very weak (see for instance the spectral analysis of Fig. 6 in Bosse et al. (2020) and references herein). The *DoLP* observed for almucantars in these two lines are therefore associated with large error bars. This in turn also affects the uncertainty level for the *AoLP*. The changes of their *DoLPs* with the azimuth appear rather flat, but are also less tightly constrained. Combined with the stronger limitation of the single scattering approach towards short wavelengths, it explains that the model fails at predicting the low values of the *DoLP* observed in the direction of Grenoble at these two wavelengths. Furthermore, ground emissions maps are less sensitive in these wavelengths (Miller et al., 2013), so that the map used in the model might also differ from the real emissions.

Examination of Figure 8 shows that, without any contribution from the background or aerosols, significantly larger values of the *DoLP* are modeled in the green line (557.7 nm). The blue (427 nm) and the orange lines (620 nm) behave similarly. For these three wavelengths, the measured radiant fluxes are fitted when adding the 1-low aerosol model and respectively 114% (Figure 10), 213% (Figure 11) and 43% (Figure 12) of natural background radiant flux (integrated star light and/or nightglow, plus the effect of MS). The percentages are calculated with respect to the maximum radiant flux measured by the instrument around azimuth $a = 260^\circ$. Interestingly, for these three colours we now reproduce also the minima and maxima of the observed *DoLP* along one almucantar, without adding any further complexity to the model. If slight discrepancies remain for the shape of $DoLP(a)$ between the model and measurements for the blue line, this characteristic is very convincingly reproduced by the model in the green and orange lines.

It is striking that we manage to replicate these observations with our model in three different wavelengths simultaneously, as they are affected differently by light pollution, the natural background from the sky, not speaking of MS. Indeed, there exist some orange emissions in the star light and in the mesospheric nightglow (Bellisario et al., 2014, 2020). The green and the blue lines exist both in the stellar light and the natural nightglow originating in thermospheric / ionospheric emissions. From Broadfoot & Kendall (1968), the orange is the tiniest of the three. The blue in the urban light spectrum is much dimmer than the green or the orange. These considerations are compatible with our results.

Finally, the misfit in the *DoLP* observed for shorter wavelengths (turquoise and purple) might require adjusted aerosol profiles (see e.g. Bergstrom et al., 2003, Figure 3). For example a different size distribution which would influence differently the shorter and the longer wavelengths. This would demand a thorough study of aerosols contribution, which is out of the scope of this paper. It is also likely related to the stronger impact of MS towards short wavelengths (see Section 4.4).

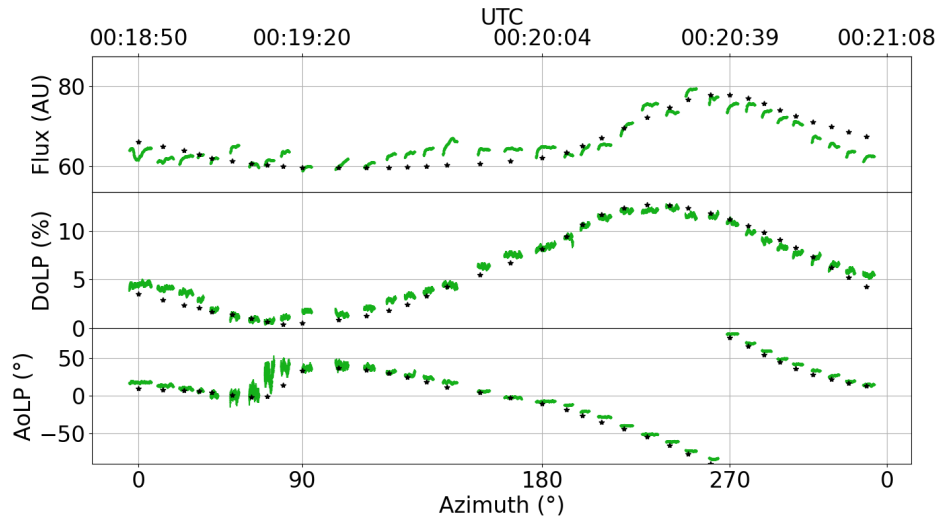


Figure 10: Almicantar in the green line. Measured data are shown in green, the width of the lines indicating the errorbars. Errors on the azimuth due to the pointing direction are of the order of a few degrees (not shown). Model predictions (black stars) are obtained with the 1-low aerosol profile plus an unpolarized, isotropic background skylight adjusted so as to fit the radiant flux (see text).

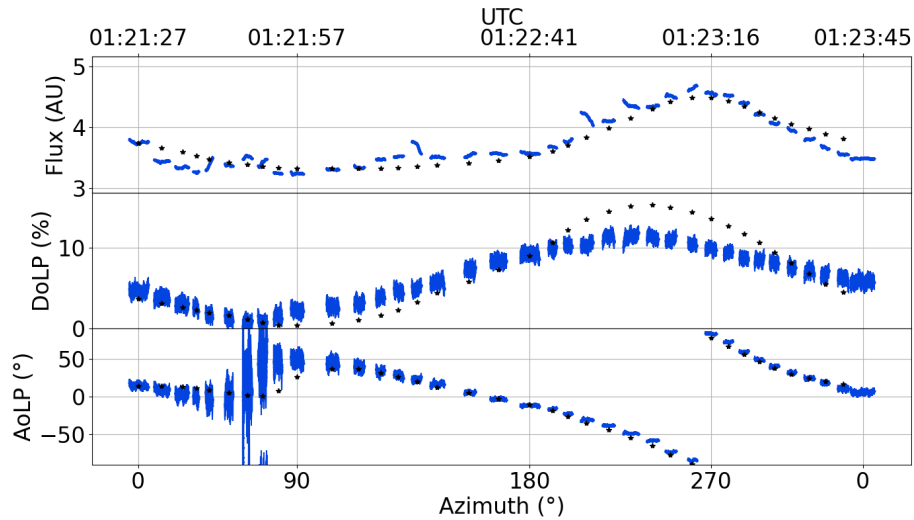


Figure 11: Same as Figure 10 for the blue line.

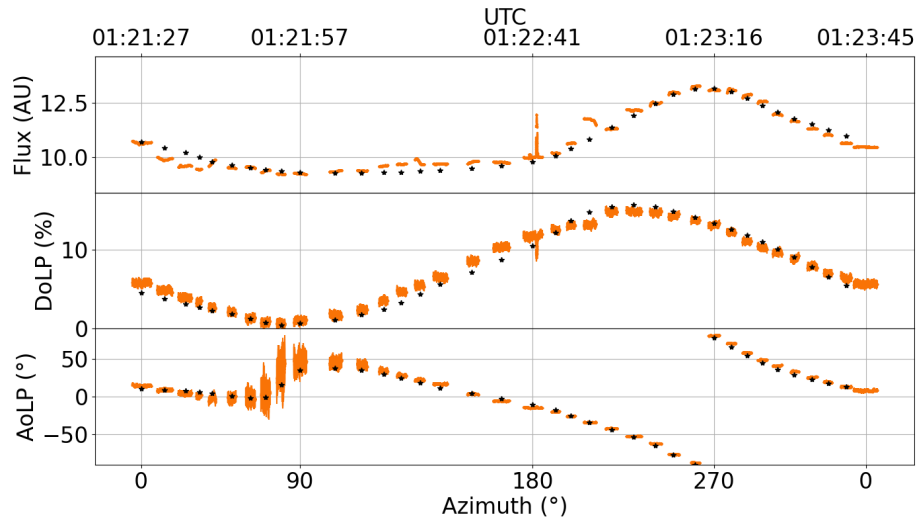


Figure 12: Same as Figure 10 for the orange line.

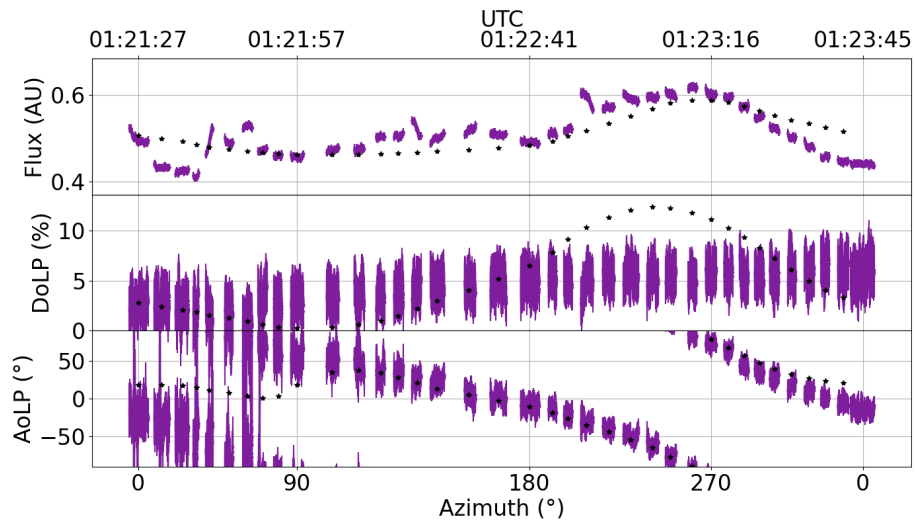


Figure 13: Same as Figure 10 for the purple line.

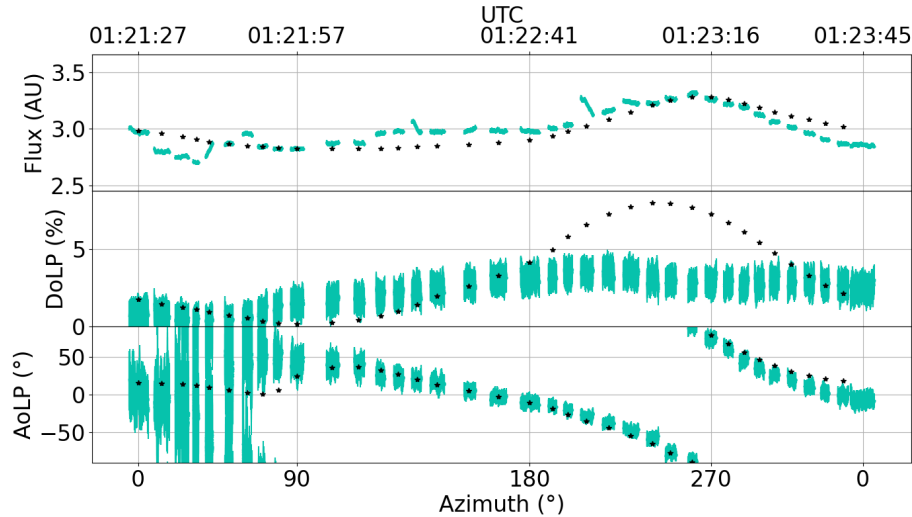


Figure 14: Same as Figure 10 for the turquoise line.

6 Discussion

We have presented in this study a polarized radiative transfer model in the single scattering approximation, which can account for a spread light pollution from the ground (including the surrounding topography), natural skylights (from stars or the nightglow) and the effect of aerosols. To our knowledge, it is the first time that such a radiative transfer code, that combines Rayleigh and Lorenz-Mie scattering, is applied to answer the question of the nightlight and its polarization. We have confronted this model to measurements performed at mid-latitudes in the French Alps in five different wavelengths, either within or outside the lines of emissions for the natural nightglow. We obtain a convincing comparison between the model outputs and the observations of the relative radiant flux, degree and angle of the linear polarization in the three wavelengths with the highest signal-to-noise ratio (green, orange and blue lines).

The results presented in this paper show the feasibility of nocturnal polarization measurements and modelisation. Our model, although currently limited to a single scattering scheme, is doomed to evolve, and constitutes a proof of concept that paves the way to further investigations of the night-sky light polarization.

Our results show that several contributions must be considered in order to explain observations: extended sources on the ground (light pollution from the nearby cities) and sources in the sky (the background) via two possible mechanisms (starlight and nightglow), plus a correction for multiple scattering. Furthermore, the atmospheric model must include Rayleigh scattering and Lorenz-Mie scattering by aerosols. We discuss below several potential applications of this model.

First, it will be used to interpret properties of the polarized lights measured at high latitudes under auroral conditions (Bosse et al., 2020), to validate or not a polarization when these are emitted in the ionosphere (Lilensten et al., 2016). The present study shows that the use of wavelengths outside the ionospheric emissions lines is crucial to determine a correct profile of aerosols, as this latter is of prime importance to understand the measured radiant flux and *DoLP*. Furthermore, in auroral conditions, ionospheric lights will strongly dominate over the integrated starlight. As a consequence, the complex picture of these emissions (2D maps) will be needed as an entry of the model. We can also imagine that in these countries

690 where wide areas are covered with snow, the reflection of auroras on the ground might be of
691 importance. These effects will be accounted for in an upcoming study.

692 In the above interpretation of mid-latitude observations, considering an unpolarized
693 background source and the 1-low aerosol model seem compulsory to explain most of our
694 measurements. It is difficult at this stage to reach a definitive conclusion on its origin, be-
695 cause we lack an absolute measure of the radiant flux. However, in the absence of any other
696 source, we have shown that our code can also handle a polarized background source, and that
697 its signature (if any) should be detectable despite the Rayleigh and Lorenz-Mie scattering. We
698 have shown that a horizontally polarized uniform sky source produces *AoLP* changes along an
699 almucantar that resemble to the ones produced by scattering within the atmosphere. It might
700 thus be insightful to consider the possibility of the polarization by horizontal ionospheric elec-
701 trical currents. These can be partially reconstructed from ground-based magnetometers (e.g.
702 Amm & Viljanen, 1999; Pulkkinen et al., 2003). This possibility is motivated by the obser-
703 vation of coherent fluctuations in time series for both the polarization parameters of auroral
704 lights, and the electron density content in the ionosphere (Bosse et al., 2020). This may have
705 further consequences for the study of the equatorial airglow, below the electrojet.

706 We have shown that the relative contribution of background lights to scattering strongly
707 varies with the wavelength: from +43% for the longest one (orange), to +114% in the green
708 and +219% in the shortest one (blue). Measuring how much this means in absolute units
709 would require the knowledge of the city light spectrum (that is not provided with the input
710 maps) as well as the instrument transfer function (such a calibration would require a dedi-
711 cated study, as it depends on the photo-sensors and on the opacity of the filters used in the
712 instrument). This higher background contribution at shorter wavelengths can be a sign that
713 the uniform, isotropic and unpolarized background partly corrects for the effect of multiple
714 scattering. Indeed, its contribution is expected to be higher at short wavelengths. This result
715 is also compatible with the expected relative contributions from the city lamps, the nightglow
716 and the starlight. On the one hand, the city contribution is likely higher in the green and or-
717 ange than in the blue (i.e. the same sky emission for all three lines should lead to a relatively
718 higher contribution for the blue). On the other hand, if we were to detect a contribution from
719 the nightglow, we would expect relatively higher radiant fluxes in the blue and green than in
720 the orange (which is not emitted in the ionosphere), for a constant contribution of the cities
721 at the observation point. Thus our results are fully compatible with the nightglow emissions,
722 showing that the method may be used for such studies. Moreover, adjusting the modeling
723 to the observations requires a contribution from the integrated starlight (at least that for the
724 orange). The combined contributions of the nightglow and the starlights can therefore be de-
725 tected with this method even in the presence of light pollution, although we cannot distinguish
726 yet between the two sources.

727 Another major result is the influence of the aerosols. The good fit between the model and
728 the measurements at several wavelengths comes with a determination of the size distribution,
729 profile distribution and refractive index of the aerosols. Any attempt to change drastically these
730 parameters degrades the fit. The precise determination of the aerosol parameters is out of scope
731 of this preliminary study. It would require for example using independent measurements (such
732 as LIDAR) or dedicated inversion schemes in order to optimize the input model parameters.
733 Nevertheless, we showed that the measurement of the light polarization constitutes an original
734 way for aerosol studies at night.

735 Of course our model suffers from limitations, the first of which being the omission of
736 multiple scattering. However, we have shown that this can be partly accounted for via the
737 unpolarized isotropic background for the blue and longer wavelengths, without ruling out
738 our model. Then, pollution maps are not provided for all wavelengths (but these might be
739 calibrated with in situ measurements). Also, although we found that an isotropic sky was
740 enough to fit our observations in the green and orange lines, a more complex model of starlight
741 and nightglow that takes into account variations in time and space could further improve the
742 model.

Nevertheless, our results suggest that our single-scattering polarized radiative transfer model together with our polarimeter may be used during night-time to detect light pollution even in remote areas, and to diagnose the aerosol content with for instance potential applications concerning the quality of air. The experimental technique is passive, contrary to lidars, low power consumption (less than 5 W), fully transportable in a suitcase, and can use any kind of visible source (artificial or natural such as the moon, the skylight, the airglow). These polarimeters may be deployed over a large area, thus allowing in the future a global coverage.

Acknowledgments

This work was partly funded by the French polar institute IPEV under program POLARLIS 3, number 1026. It was also funded by the Prematuration CNRS program and by the Maturation program CM180023, project PTCU Number 180018M from the SATT company Linksium. The polarimeter is patented by the CNRS and valorised by Linksium (international patent number 1873378). We thank the Programme National Soleil-Terre for its financial support. NG was partially supported by the French Centre National d'Etudes Spatiales (CNES) for the study of Earth's core dynamics in the context of the Swarm mission of ESA.

We thank Pierre Simoneau (ONERA) for usefull discussions on the mesospheric nightglow.

The source code will be freely available online as opensource as soon as it is documented and portable. Ground emission maps are available here: <https://eogdata.mines.edu/products/vn1/>

Atmospheric profiles are available here: <http://eodg.atm.ox.ac.uk/RFM/atm/>

Elevation data are available here: <https://www.eorc.jaxa.jp/ALOS/en/aw3d30/index.htm>

References

- Amm, O., & Viljanen, A. (1999). Ionospheric disturbance magnetic field continuation from the ground to the ionosphere using spherical elementary current systems. *Earth, Planets and Space*, *51*(6), 431–440.
- Banks, P. M., & Kockarts, G. (1973). *Aeronomy*. Springer.
- Bellisario, C., Keckhut, P., Blanot, L., Hauchecorne, A., & Simoneau, P. (2014, June). O₂ and OH night Airglow emissions derived from GOMOS-EnvisatInstrument. *Journal of Atmospheric and Oceanic Technology*, *31*(6), 1301-1311. doi: 10.1175/JTECH-D-13-00135
- Bellisario, C., Simoneau, P., Keckhut, P., & Hauchecorne, A. (2020, March). Comparisons of spectrally resolved nightglow emission locally simulated with space and ground level observations. *Journal of Space Weather and Space Climate*, *10*, 21. doi: 10.1051/swsc/2020017
- Bergstrom, R. W., Pilewskie, P., Schmid, B., & Russell, P. B. (2003). Estimates of the spectral aerosol single scattering albedo and aerosol radiative effects during safari 2000. *Journal of Geophysical Research: Atmospheres*, *108*(D13).
- Berk, A., Conforti, P., Kennett, R., Perkins, T., Hawes, F., & Van Den Bosch, J. (2014). Modtran® 6: A major upgrade of the modtran® radiative transfer code. In *2014 6th workshop on hyperspectral image and signal processing: Evolution in remote sensing (whispers)* (pp. 1–4).
- Bommier, V., Sahal-Brechot, S., Dubau, J., & Cornille, M. (2011). The theoretical impact polarisation of the O I 6300 Å red line of Earth Aurorae. , 9.

- 794 1, 4.3
- 795 Born, M., & Wolf, E. (1999). *Principles of optics : electromagnetic theory of propagation,*
- 796 *interference and diffraction of light.*
- 797 3.1.4, 4.2, Appendix A
- 798 Bosse, L., Liliensten, J., Gillet, N., Rochat, S., Delboulbé, A., Curaba, S., ... Frédérique, A.
- 799 (2020). On the nightglow polarisation for space weather exploration. *Submitted to the*
- 800 *Journal of Space Weather and Space Climate,* -.
- 801 1, 2, 4.3, 9, 5.1.1, 5.2, 6
- 802 Broadfoot, A. L., & Kendall, K. R. (1968, January). The airglow spectrum, 3100-10,000 Å.
- 803 *Journal of Geophysical Research,* 73(1), 426–428. doi: 10.1029/JA073i001p00426
- 804 5, 5.2
- 805 Bucholtz, A. (1995, May). Rayleigh-scattering calculations for the terrestrial atmosphere.
- 806 *Applied Optics,* 34(15), 2765–2773. doi: 10.1364/AO.34.002765
- 807 Appendix A, Appendix A, A1, Appendix A, Appendix A
- 808 Burrows, J. P., Richter, A., Dehn, A., Deters, B., Himmelmann, S., Voigt, S., & Orphal,
- 809 J. (1999, March). Atmospheric remote-sensing reference data from gome—2.
- 810 temperature-dependent absorption cross sections of 3 in the 231–794nm range. *Jour-*
- 811 *nal of Quantitative Spectroscopy and Radiative Transfer,* 61(4), 509–517. doi:
- 812 10.1016/S0022-4073(98)00037-5
- 813 Appendix A
- 814 Chandrasekhar, S. (1960). *Radiative Transfer.* Dover Publications Inc. Retrieved 2020-02-
- 815 07, from <http://archive.org/details/RadiativeTransfer>
- 816 Appendix A, Appendix A
- 817 de Haan, J. F., Bosma, P., & Hovenier, J. (1987). The adding method for multiple scattering
- 818 calculations of polarized light. *Astronomy and astrophysics,* 183, 371–391.
- 819 4.4
- 820 Dubovik, O., Smirnov, A., Holben, B. N., King, M. D., Kaufman, Y. J., Eck, T. F., &
- 821 Slutsker, I. (2000). Accuracy assessments of aerosol optical properties retrieved from
- 822 Aerosol Robotic Network (AERONET) Sun and sky radiance measurements. *Journal of*
- 823 *Geophysical Research: Atmospheres,* 105(D8), 9791–9806. doi: 10.1029/2000JD900040
- 824 3.1.4
- 825 Dymond, K. F., Nicholas, A. C., Budzien, S. A., Stephan, A. W., Coker, C., Hei, M. A., &
- 826 Groves, K. M. (2019, June). A Comparison of Electron Densities Derived by Tomographic
- 827 Inversion of the 135.6-nm Ionospheric Nightglow Emission to Incoherent Scatter Radar
- 828 Measurements. *Journal of Geophysical Research (Space Physics),* 124(6), 4585-4596.
- 829 doi: 10.1029/2018JA026412
- 830 1
- 831 Evans, K. F., & Stephens, G. L. (1991, January). A new polarized atmospheric radiative
- 832 transfer model. *Journal of Quantitative Spectroscopy and Radiative Transfer,* 46(5), 413-
- 833 423. doi: 10022-4073/91
- 834 4.4
- 835 Finlay, C. C., Olsen, N., Kotsiaros, S., Gillet, N., & Tøffner-Clausen, L. (2016, Decem-
- 836 ber). Recent geomagnetic secular variation from Swarm and ground observatories as
- 837 estimated in the CHAOS-6 geomagnetic field model. *Earth, Planets and Space,* 68(1).
- 838 doi: 10.1186/s40623-016-0486-1
- 839 4.3
- 840 Garcia-Saenz, A., Sanchez de Miguel, A., Espinosa, A., Crespo, A., Aragonés, N., Llorca,
- 841 J., ... Kogevinas, M. (2018, April). Evaluating the association between artificial light-at-
- 842 night exposure and breast and prostate cancer risk in Spain (MCC-Spain study). *Environ-*
- 843 *mental Health Perspectives,* 126. doi: 10.1289/EHP1837
- 844 1
- 845 Grubisic, M., van Grunsven, R., Kyba, C., Manfrin, A., & Hölker, F. (2018, September). In-
- 846 sect declines and agroecosystems: Does light pollution matter? *Annals of Applied Biology,*
- 847 173, 180–189. doi: 10.1111/aab.12440

- 848 1
849 Hansen, J. E. (1971). Multiple scattering of polarized light in planetary atmospheres part
850 ii. sunlight reflected by terrestrial water clouds. *Journal of Atmospheric Sciences*, 28(8),
851 1400–1426.
852 4.4
- 853 Hansen, J. E., & Hovenier, J. W. (1971, January). The doubling method applied to multiple
854 scattering of polarized light. *Journal of Quantitative Spectroscopy and Radiative Transfer*,
855 11(6), 809–812. doi: 10.1016/0022-4073(71)90057-4
856 4.4
- 857 Hansen, J. E., & Travis, L. D. (1974, October). Light scattering in planetary atmospheres.
858 *Space Science Reviews*, 16(4), 527–610. doi: 10.1007/BF00168069
859 4.4
- 860 Herman, M., Balois, J. Y., Gonzalez, L., Lecomte, P., & Lenoble, J. (1986, October). Strato-
861 spheric aerosol observations from a balloon-borne polarimetric experiment. *Applied Op-
862 tics*, 25, 3573–3584. doi: 10.1364/AO.25.003573
863 4.4
- 864 Horvath, G., Kriska, G., Malik, P., & Robertson, B. (2009, August). Polarized light pollu-
865 tion: A new kind of ecological photopollution. *Frontiers in Ecology and the Environment*,
866 7, 317–325. doi: 10.1890/080129
867 1
- 868 Hovenier, J. W. (1971, June). Multiple Scattering of Polarized Light in Planetary Atmo-
869 spheres. *Astronomy and Astrophysics*, 13, 7.
870 4.4
- 871 Jaenicke, R. (1993). Chapter 1 Tropospheric Aerosols. In *International Geophysics* (Vol. 54,
872 pp. 1–31). Elsevier. doi: 10.1016/S0074-6142(08)60210-7
873 3.1.4
- 874 King, M. D. (1986). Comparative accuracy of selected multiple scattering approximations.
875 *Journal of Atmospheric Sciences*, 43(8), 784–801.
876 4.4
- 877 Kyba, C., Kuester, T., Sanchez de Miguel, A., Baugh, K., Jechow, A., Hölker, F., . . . Guanter,
878 L. (2017, November). Artificially lit surface of Earth at night increasing in radiance and
879 extent. *Science Advances*, 3, e1701528. doi: 10.1126/sciadv.1701528
880 1
- 881 Kyba, C., Ruhtz, T., Fischer, J., & Hölker, F. (2011, December). Lunar skylight polarization
882 signal polluted by urban lighting. *Journal of Geophysical Research (Atmospheres)*, 116,
883 24106-. doi: 10.1029/2011JD016698
884 1
- 885 Lax, M. (1951). Multiple Scattering of Waves. , 23(4), 287–310. Retrieved 2021-05-
886 18, from <https://link.aps.org/doi/10.1103/RevModPhys.23.287> doi: 10.1103/
887 RevModPhys.23.287
888 4.4
- 889 Leinert, C., Bowyer, S., Haikala, L. K., Hanner, M. S., Hauser, M. G., Levasseur-Regourd,
890 A.-C., . . . Witt, A. N. (1998, January). The 1997 reference of diffuse night sky brightness.
891 *Astronomy and Astrophysics Supplement Series*, 127(1), 1–99. doi: 10.1051/aas:1998105
892 1, 3.1.3, 5
- 893 Liliensten, J., Barthélemy, M., Besson, G., Lamy, H., Johnsen, M. G., & Moen, J. (2016,
894 July). The thermospheric auroral red line Angle of Linear Polarization: Auroral angle of
895 linear polarization. *Journal of Geophysical Research: Space Physics*, 121(7), 7125–7134.
896 doi: 10.1002/2016JA022941
897 1, 6
- 898 Liliensten, J., Moen, J., Barthélemy, M., Thissen, R., Simon, C., Lorentzen, D. A., . . .
899 Sigernes, F. (2008, April). Polarization in aurorae: A new dimension for space envi-
900 ronments studies. *Geophysical Research Letters*, 35(8). doi: 10.1029/2007GL033006
901 1

- 902 Lorenz, L. (1890). Lysbevaegelsen i og uden for en af plane lysbolger belyst kugle”. det kon-
 903 gelige danske videnskabernes selskabs skrifter. 6. , 6. *Bind* (1, 1–62.
 904 3.1.4, 4.2, Appendix A
- 905 McFarlane, S. C. (1974, September). A Bethe theory for the polarization of impact radia-
 906 tion. *Journal of Physics B Atomic Molecular Physics*, 7(13), 1756-1771. doi: 10.1088/
 907 0022-3700/7/13/021
 908 3.2.1
- 909 McMaster, W. H. (1954, September). Polarization and the Stokes Parameters. *American*
 910 *Journal of Physics*, 22(6), 351-362. doi: 10.1119/1.1933744
 911 3.2.2
- 912 Mie, G. (1908). Beiträge zur Optik trüber Medien, speziell kolloidaler Metallösungen. *An-*
 913 *nalen der Physik*, 330(3), 377–445. doi: 10.1002/andp.19083300302
 914 3.1.4, 4.2, Appendix A, Appendix A
- 915 Miller, S. D., Straka, W., Mills, S. P., Elvidge, C. D., Lee, T. F., Solbrig, J., ... Weiss, S. C.
 916 (2013, December). Illuminating the Capabilities of the Suomi National Polar-Orbiting
 917 Partnership (NPP) Visible Infrared Imaging Radiometer Suite (VIIRS) Day/Night Band.
 918 *Remote Sensing*, 5(12), 6717–6766. doi: 10.3390/rs5126717
 919 3.1.2, 5.2
- 920 Mills, S., Weiss, S., & Liang, C. (2013, September). VIIRS day/night band (DNB) stray light
 921 characterization and correction. In J. J. Butler, X. J. Xiong, & X. Gu (Eds.), *SPIE Optical*
 922 *Engineering + Applications* (p. 88661P). San Diego, California, United States. doi: 10
 923 .1117/12.2023107
 924 3.1.2
- 925 Mishchenko, M. I., Travis, L. D., & Lacis, A. A. (2002). *Scattering, absorption, and emis-*
 926 *sion of light by small particles*. Cambridge University Press.
 927 Appendix A
- 928 Ougolnikov, O. S., & Maslov, I. A. (2002, May). Multicolor Polarimetry of the Twilight
 929 Sky: The Role of Multiple Light Scattering as a Function of Wavelength. *Cosmic Re-*
 930 *search*, 40(3), 224-232.
 931 4.4
- 932 Parihar, N., Radicella, S. M., Nava, B., Migoya-Orue, Y. O., Tiwari, P., & Singh, R. (2018,
 933 May). An investigation of the ionospheric F region near the EIA crest in India using OI
 934 777.4 and 630.0 nm nightglow observations. *Annales Geophysicae*, 36(3), 809-823. doi:
 935 10.5194/angeo-36-809-2018
 936 1
- 937 Plane, J., Oetjen, H., de Miranda, M., Saiz-Lopez, A., Gausa, M., & Williams, B. (2012, Jan-
 938 uary). On the sodium D line emission in the terrestrial nightglow. *Journal of Atmospheric*
 939 *and Solar-Terrestrial Physics*, 74, 181–188. doi: 10.1016/j.jastp.2011.10.019
 940 1
- 941 Pulkkinen, A., Amm, O., & Viljanen, A. (2003). Ionospheric equivalent current distributions
 942 determined with the method of spherical elementary current systems. *Journal of Geophys-*
 943 *ical Research: Space Physics*, 108(A2).
 944 6
- 945 Pust, N. J., & Shaw, J. A. (2011). Comparison of skylight polarization measurements and
 946 MODTRAN-P calculations. *Journal of Applied Remote Sensing*, 5, 18.
 947 4, 4.4
- 948 Ramella-Roman, J. C., Pohl, S. A., & Jacques, S. L. (2005). Three monte carlo programs of
 949 polarized light transport into scattering media: part i. *Optics Express*, 13(12), 4420–4438.
 950 4.4
- 951 Rayleigh, J. W. S. B. (1871). On the scattering of light by small particles. *The London, Edin-*
 952 *burgh, and Dublin Philosophical Magazine and Journal of Science*, 41, 447—454. doi: 10
 953 .1080/14786447108640507
 954 Appendix A

- 955 Remedios, J., Leigh, R., Waterfall, A., Moore, D., Sembhi, H., Parkes, I., ... Hauglustaine,
 956 D. (2007). Mipas reference atmospheres and comparisons to v4. 61/v4. 62 mipas level
 957 2 geophysical data sets. *Atmospheric Chemistry and Physics Discussions*, 7(4), 9973–
 958 10017.
 959 3.1.4
- 960 Santer, R., Herman, M., Tanre, D., & Lenoble, J. (1988, November). Characterization of
 961 stratospheric aerosol from polarization measurements. *Journal of Geophysical Research:
 962 Atmospheres*, 93(D11), 14,209-14,221. doi: 10.1029/JD093iD11p14209
 963 4.4
- 964 Staude, H. (1975). Scattering in the earth's atmosphere: Calculations for milky way and zo-
 965 diaical light as extended sources. *Astronomy and Astrophysics*, 39, 325.
 966 3.1.3, 4.4
- 967 Tadono, T., Nagai, H., Ishida, H., Oda, F., Naito, S., Minakawa, K., & Iwamoto, H. (2016,
 968 June). *Generation of the 30 m-mesh global digital surface model by alos prism* (Vol. XLI-
 969 B4). <https://doaj.org>. Copernicus Publications. doi: 10.5194/isprs-archives-XLI-B4-157
 970 -2016
 971 3.1.5
- 972 Tashchilin, A., & Leonovich, L. (2016, September). Modeling nightglow in atomic oxygen
 973 red and green lines under moderate disturbed geomagnetic conditions at midlatitudes.
 974 *Solar-Terrestrial Physics*, 2(4), 94-106. doi: 10.12737/21491
 975 1
- 976 Ugolnikov, O. S., Postlyakov, O. V., & Maslov, I. A. (2004, September). Effects of mul-
 977 tiple scattering and atmospheric aerosol on the polarization of the twilight sky. *Journal of
 978 Quantitative Spectroscopy Radiative Transfer*, 88, 233-241. doi: 10.1016/j.jqsrt.2003.12
 979 .033
 980 4.4
- 981 van de Hulst, H. C. (1981). *Light scattering by small particles*. New York: Dover Publica-
 982 tions.
 983 3.1.4, 3.2.2
- 984 Vargas, F. (2019, November). Traveling Ionosphere Disturbance Signatures on
 985 Ground-Based Observations of the O(¹D) Nightglow Inferred From 1-D Model-
 986 ing. *Journal of Geophysical Research (Space Physics)*, 124(11), 9348-9363. doi:
 987 10.1029/2019JA027356
 988 1
- 989 Zielinska-Dabkowska, K. (2018, January). Make lighting healthier. *Nature*, 553. doi: 10
 990 .1038/d41586-018-00568-7
 991 1

Appendix A Computation of the radiant flux measured by our virtual instrument

In this appendix, we compute the radiant flux measured by a virtual instrument in A when the light is emitted by a single point source E , and scattered at a single point R along the line of sight (see Figure 2). We describe each intermediate step in order for the reader to understand and reproduce our results.

We use here the units used by POMEROL, with the scale factor implemented in the code. The scale factor has no effect on the dimensional analysis, but are kept here for more transparency on the code.

First, the source is fully described by its radiance L_E in $\text{nW}/\text{m}^2/\text{sr}$ as given by the input map (see section 3.1), and its surface area A_E in km^2 . It is considered small enough to be approximated as a point source of radiant intensity $I_E = L_E A_E$ in nW/sr . Its emission is considered isotropic. From this, the irradiance reaching the scattering volume in R is (in nW/m^2):

$$E_E = L_E \Omega_E \exp(-\tau_{ER}) \quad (\text{A1})$$

$$= L_E \frac{A_E}{d_{ER}^2} \exp(-\tau_{ER}) \quad (\text{A2})$$

where $\Omega_E = A_E/d_{ER}^2$ is the solid angle of the emission surface as seen from the scattering point at a distance d_{ER} (in km), and τ_{ER} is the effective optical depth of the atmosphere between the emission in E and the scattering in R (see equations A21 to A24).

The radiant intensity I_R (in nW/sr) scattered by the volume Γ of air or aerosol around R is:

$$I_R = E_E \sigma \frac{\Phi(\theta)}{4\pi} \quad (\text{A3})$$

where σ (in km^2) is the total scattering coefficient, θ is the scattering angle and $\Phi(\theta)$ is the scattering phase function of the molecules or particles (see equation A5 and following text). By definition the phase function Φ is dimensionless and normalized across a sphere (e.g. Mishchenko et al. (2002); Chandrasekhar, S. (1960)), such that, Ω being a solid angle:

$$1 = \frac{1}{4\pi} \int_{\Omega} \Phi(\Omega) d\Omega \quad (\text{A4})$$

It ensues that $\Phi(\theta)/(4\pi)$ has units of sr^{-1} . The phase function Φ and total scattering coefficient σ to consider is different whether we consider Rayleigh scattering on air molecules or Lorenz-Mie scattering on aerosols.

$$\Phi_{ray}(\theta) = \frac{3}{4} (1 + \cos^2 \theta) \quad (\text{A5})$$

is the Rayleigh phase function (Bucholtz, 1995). It does not take into account molecular anisotropy effects. This approximation does not affect our results significantly, but could be improved in the future if necessary using a formula from Chandrasekhar (Chandrasekhar, S., 1960). The aerosol phase function $\Phi_{aer}(\theta)$ is computed using Lorenz-Mie scattering theory (Lorenz, 1890; Mie, 1908; Born & Wolf, 1999) and depends on the aerosol model parameters listed in Table 1. For the air molecules, the total scattering coefficient is

$$\sigma_{ray} = \beta \Gamma \quad (\text{A6})$$

and for the aerosols, it is:

$$\sigma_{aer} = \bar{\omega} C_{ext} \Gamma \quad (\text{A7})$$

with β the Rayleigh scattering volume coefficient in km^{-1} as described in Bucholtz (1995) (see equations A18 to A20), $\bar{\omega}$ the single scattering albedo of the aerosol, C_{ext} the extinction coefficient of the aerosol in km^{-1} and Γ the scattering volume in km^3 . Γ , the scattering volume

Coefficient	$0.2 < \lambda (\mu m) < 0.5$	$0.5 < \lambda (\mu m)$
A_{ray}	7.68246×10^{-4}	10.21675×10^{-4}
A_{op}	6.49997×10^{-3}	8.64145×10^{-3}
B	3.55212	3.99668
C	1.35579	0.00110298
D	0.11563	0.0271393

Table A1: Parameters used in equation (A20). (Bucholtz, 1995)

1038 centered around R (see Fig. 2), is a truncated cone defined by ε the half aperture angle of the
 1039 virtual instrument (similar to that of the real polarimeter), d_{AR} and l the half-height of the cone.
 1040 It is given by

$$1041 \quad \Gamma = \frac{\pi}{3} \tan^2(\varepsilon) l (3d_{AR}^2 - l^2/4) . \quad (A8)$$

1042 Finally, the radiant flux in nW measured by the virtual instrument in A is:

$$1043 \quad F_A = I_R \Omega_A \exp(-\tau_{AR}) \quad (A9)$$

$$1044 \quad = \frac{I_R \Sigma}{d_{AR}^2} \exp(-\tau_{AR}) \quad (A10)$$

1045

1046 Where Ω_A is the solid angle (in sr) of the detector as seen from the scattering volume in R , Σ
 1047 is the surface area of the detector (in m²), d_{AR} is the distance from the scattering point to the
 1048 detector (in km) and τ_{AR} is the effective optical depth along the path from R to A . Developing
 1049 I_R into the initial parameters gives us:

$$F_A = I_R \frac{\Sigma}{d_{AR}^2} \exp(-\tau_{AR}) \quad (A11)$$

$$= E_E \sigma \frac{\Phi(\theta)}{4\pi} \frac{\Sigma}{d_{AR}^2} \exp(-\tau_{AR}) \quad (A12)$$

$$= L_E \frac{A_E}{d_{ER}^2} \exp(-\tau_{ER} - \tau_{AR}) \sigma \frac{\Phi(\theta)}{4\pi} \frac{\Sigma}{d_{AR}^2} \quad (A13)$$

$$= \frac{L_E A_E \Sigma}{4\pi d_{ER}^2 d_{AR}^2} \exp(-\tau_{ER} - \tau_{AR}) \sigma \Phi(\theta) \quad (A14)$$

At this point, we replace the scattering coefficient by the corresponding expression, whether we consider the Rayleigh scattering on air molecules, or the Mie scattering on aerosols. This gives:

$$F_A^{ray} = \frac{L_E A_E \Sigma}{4\pi d_{ER}^2 d_{AR}^2} \exp(-\tau_{ER} - \tau_{AR}) \Gamma \beta \Phi_{ray}(\theta) \quad (A15)$$

and:

$$F_A^{aer} = \frac{L_E A_E \Sigma}{4\pi d_{ER}^2 d_{AR}^2} \exp(-\tau_{ER} - \tau_{AR}) \Gamma \bar{\omega} C_{ext} \Phi_{aer}(\theta) \quad (A16)$$

The total radiant flux measured by our virtual instrument is then the sum of both contributions as:

$$F_A = \frac{L_E A_E \Sigma}{4\pi d_{ER}^2 d_{AR}^2} \Gamma \exp(-\tau_{ER} - \tau_{AR}) [\beta \Phi_{ray}(\theta) + \bar{\omega} C_{ext} \Phi_{aer}(\theta)] \quad (A17)$$

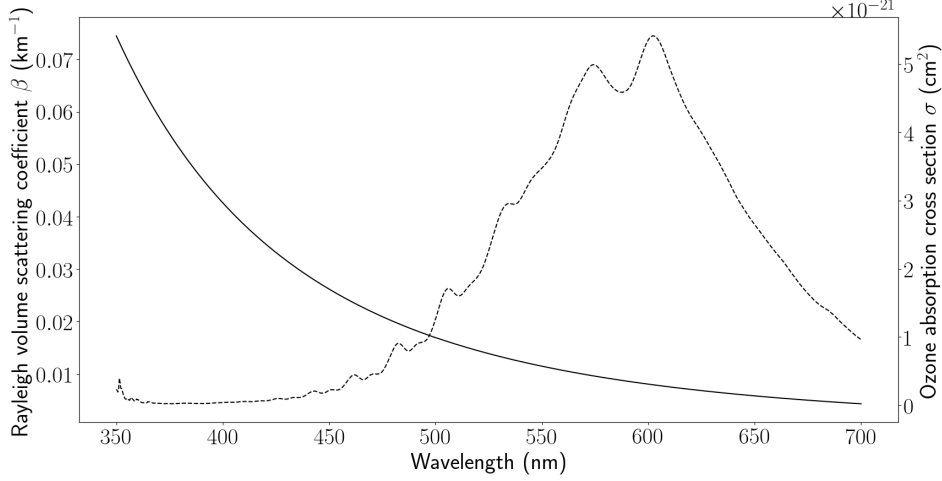


Figure A1: Rayleigh volume scattering coefficient at sea level $\beta_0(\lambda) = \beta(\lambda, z)|_{z=0}$ (full line, left, see equation A19), and ozone absorption cross section $\sigma_{O_3}(\lambda)$ (dashed line, right), as a function of wavelength.

1050 We describe below in more detail the computations of all the physical quantities used
 1051 to compute F_A . Classically, the Rayleigh scattering cross section per molecule is (Rayleigh,
 1052 1871; Mie, 1908; Bucholtz, 1995):

$$1053 \quad c^{ray} = \frac{24\pi^3}{\lambda^4 N_s^2} \left(\frac{m_s^2 - 1}{m_s^2 + 2} \right)^2 \frac{6 + 3\rho_n}{6 - 7\rho_n}, \quad (A18)$$

1054 with λ the wavelength, N_s the molecular number density for standard air, m_s the refractive
 1055 index of standard air at λ and ρ_n the depolarization factor. In our model, this is accounted for
 1056 via the Rayleigh volume scattering coefficient $\beta(\lambda, z)$ (in km^{-1}). Following Bucholtz (1995),
 1057 it is approximated as

$$1058 \quad \beta(\lambda, z) = \beta_0(\lambda) \frac{P(z)}{P_0} \frac{T_0}{T(z)}, \quad (A19)$$

1059 with $P(z)$ and $T(z)$ the atmospheric pressure and temperature profiles. $P_0 = 101\,325$ Pa and
 1060 $T_0 = 288.15$ K are the pressure and temperature at sea level, and

$$1061 \quad \beta_0(\lambda) = A_{ray} \lambda^{-(B+C\lambda+D/\lambda)}, \quad (A20)$$

1062 with λ the wavelength (in μm). This approximation takes into account the depolarization (or
 1063 King) factor. Values for coefficients A_{ray} , B , C and D are given in Table A1, and $\beta(\lambda, z)|_{z=0}$ is
 1064 shown in Figure A1.

1065 The effective optical depth τ of the atmosphere between E and R (and similarly between
 1066 R and A), is the sum of three contributions from Rayleigh scattering, ozone absorption and
 1067 aerosol extinction:

$$1068 \quad \tau = \tau_{ray} + \tau_{O_3} + \tau_{aer}. \quad (A21)$$

1070 The optical depth from Rayleigh scattering between E and R is

$$1071 \quad \tau_{ray}(z, \lambda) = \frac{\tau_0(\lambda)}{P_0} \int_E^R P(z') dz', \quad (A22)$$

1073 where $\tau_0(\lambda)$ follows equation (A20) with A_{ray} replaced by A_{op} (value given in Table A1). The
 1074 optical depth for ozone absorption is

$$1075 \tau_{O_3}(z, \lambda) = \sigma_{O_3}(\lambda) \int_E^R N_{O_3}(z') dz', \quad (A23)$$

1076

1077 where $N_{O_3}(z)$ is the ozone number density at altitude z (provided with the atmospheric profile,
 1078 see Figure 1) and $\sigma_{O_3}(\lambda)$ (shown in Figure A1) is the ozone absorption cross section at wave-
 1079 length λ and a fixed temperature of 273 K (Burrows et al., 1999). This is an approximation
 1080 which could be refined in future versions with a dependence on temperature. The optical depth
 1081 for aerosols is

$$1082 \tau_{aer}(z, \lambda) = \int_E^R C_{ext}^{aer}(z', \lambda) dz'. \quad (A24)$$

1083

1084